energy&fuels

Article

pubs.acs.org/EF

Impacts of Mineral Reaction Kinetics and Regional Groundwater Flow on Long-Term CO_2 Fate at Sleipner

Guanru Zhang,[†,‡] Peng Lu,[‡,§] Xiaomei Wei,[*,†] and Chen Zhu[*,‡]

[†]College of Water Resources and Architectural Engineering, Northwest A&F University, Yangling 712100, China

[‡]Department of Geological Sciences, Indiana University, Bloomington, Indiana 47408, United States

[§]EXPEC Advanced Research Center, Saudi Aramco, Dhahran 31311, Saudi Arabia

ABSTRACT: We conducted coupled reactive mass transport modeling of CO_2 storage in a sandy aquifer resembling the uppermost layer in the Utsira Sand, Sleipner, North Sea, in order to investigate the general effects of rate laws and regional groundwater flow on long-term CO_2 fate in saline aquifers. The temporal and spatial evolution of CO_2 plume and the fate of injected CO_2 were simulated with a series of scenarios with different rate law formulations for dissolution and precipitation reactions and different flow regimes. The results indicated the following: (1) Changing the dissolution rate laws of the main soluble silicate minerals can influence the silicate reactions and mineral trapping by impacting the sensitivity of the relevant coupled reaction's rate to the acidification of brine. The steeper the slope of rate$-\Delta G_r$ (Gibbs free energy of reaction) relationships, the more sensitive the coupled reaction rate and the mineral trapping are to the acidification of brine. The predicted fraction of CO_2 mineral trapping when using the linear rate law for feldspar dissolution is twice as much as when using the nonlinear rate law. (2) Mineral trapping is more significant when regional groundwater flow is taken into consideration. Under the influence of regional groundwater flow, the replenishment of fresh brine from upstream continuously dissolves CO_2 at the tail of CO_2 plume, generating a larger acidified area where mineral trapping takes place. In a Sleipner-like aquifer, the upstream replenishment of groundwater results in ∼22% mineral trapping at year 10 000, compared to ∼4% when the effects of regional groundwater are ignored. (3) Using linear rate law for silicate dissolution reactions can exaggerate the effect of groundwater flow on the reaction rates and mineral trapping and can overestimate the theoretical mineral trapping capacity, compared to using the nonlinear rate law.

1. INTRODUCTION

Underground sequestration of carbon dioxide, in particular, sequestration in saline aquifers, given their massive storage capacity and extensive geographic distribution, is one of the most promising options for the mitigation of greenhouse gas through reducing the release rate of CO_2 to the atmosphere.[1,2] CO_2 can be trapped in underground reservoirs by four storage mechanisms: (1) structural trapping; (2) residual CO_2 trapping; (3) solubility trapping; and (4) mineral trapping.[3] Of these four options, mineral trapping is considered the safest mechanism in long-term storage of CO_2.[4]

To date, the effects of kinetic parameters, such as rate constant and reactive surface area, on carbon storage have been widely studied.[5−10] However, the effects of rate laws on the long-term fate of CO_2 storage have rarely been explored. Numerous experiments have shown that the traditional linear rate law which is generally applied in the reactive transport modeling of CO_2 sequestration deviates from the observed nonlinear relationship between reaction rates and Gibbs free energy of the reaction.[11−24]

We investigated the effect of different rate laws on CO_2 trapping in a sandy aquifer resembling the Mt. Simon formation in the U.S. Midwest[25] and found that long-term mineral trapping is sensitive to rate laws for feldspar dissolution. If using nonlinear rate law for feldspar dissolution in place of the traditional linear rate law, then the mineral trapping fraction at year 10 000 decreases from ∼45 to ∼22% because of the reduced dissolution rate of feldspar. However, we only studied the feldspar group for the dissolution rate law in the above-mentioned study. In addition, different saline aquifers are of different initial sandstone compositions, water chemistry, and reservoir conditions, which may affect the specific geochemical reactions and the role of the rate laws on long-term fate of injected CO_2. Therefore, it is necessary to study the effect of mineral rate laws for a different CO_2 storage site and extend the investigation to primary minerals other than feldspars.

Although some researchers considered regional groundwater in the reactive transport modeling of the CO_2 sequestration,[25−28] the detailed quantitative analysis of its impact on the long-term fate of the injected CO_2 is still lacking. Liu et al.[26] discussed the influence of regional groundwater flow on long-term fate of CO_2 at the Mt. Simon formation with 1D radial model and the groundwater flow rate of 0.3 m/yr. They found that groundwater flow can facilitate the dissolution of the injected CO_2 and can greatly influence the mass partition of CO_2. Aradóttir et al.[27] used a groundwater flow velocity of 25 m/yr in the 2D and 3D model for exploring the short-term reactive transport (∼10−100 years) of CO_2 stored in basalts formation (400−800 m depth) at the Hellisheidi geothermal field, Iceland. However, both Liu et al.[26] and Aradóttir et al.[27] did not investigate the effects of the flow velocity variations on the fate of the injected CO_2. Tutolo et al.[28] set the background

Received: October 29, 2015
Revised: February 26, 2016
Published: April 7, 2016

DOI: 10.1021/acs.energyfuels.5b02556
Energy Fuels 2016, 30, 4159−4180

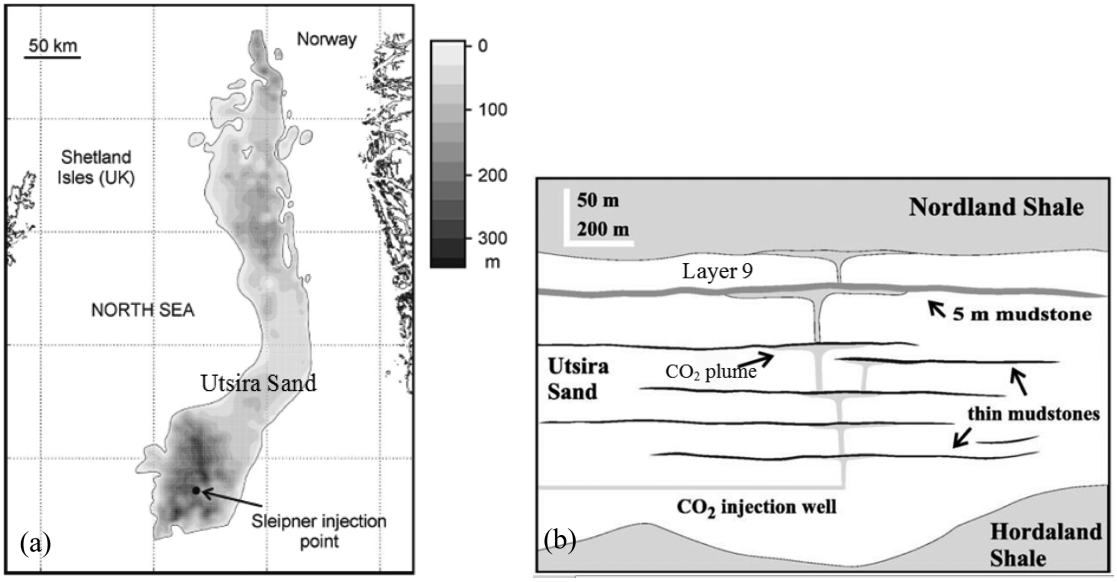

Figure 1. (a) Limits and thickness of the Utsira Sand and planimetric location of the CO_2 injection point.[40] (b) Schematic illustration of CO_2 injection at Sleipner and rising CO_2 plumes being partially trapped under thin mudstones before reaching Nordland Shale cap rock.[86] Layer 9 is in immediate contact with the overlying sealing caprock, and the injection well is located at 1012 m below the mean sea level. Note the vertical exaggeration.

groundwater velocity to be 1.1, 5.5, and 10.9 m/yr in the short-term reactive transport simulations (50 years) for the cool CO_2 injection into a 100 °C calcite or dolomite reservoir with the pressure of 20 000 kPa. They found that higher groundwater velocity can push the CO_2 plume out of the simulated region quicker, which results in a smaller amount of calcite dissolution. The limitations in Tutolo et al.[28] were that the simulated region was not large enough to cover the entire CO_2 plume and that only calcite and dolomite were considered as reactive minerals in their model.

To investigate the effect of the dissolution and precipitation rate laws and the regional groundwater flow on long-term CO_2 sequestration (especially on mineral trapping) in a different sandy aquifer other than Mt. Simon, we chose the Sleipner in Norway as our field site. In this study, the effects of the dissolution rate law of silicate minerals other than feldspars were also assessed.

The Sleipner project, situated in the Norwegian North Sea, is the world's first industrial-scale geological carbon storage project. Starting in 1996, CO_2 separated from natural gas has been injected into the Utsira Sand (Figure 1a) at a rate of approximately 1 million metric tons of CO_2 per year.[29] A total of ~13.5 Mt of CO_2 had been injected by the middle of 2012.[30] Our current study only focuses on the CO_2 storage in the uppermost layer (Layer 9) of the Utsira Sand formation because the CO_2 plume in Layer 9 (Figure 1b) is more clearly resolved by using high-resolution seismic maps than the lower eight CO_2 plume layers. Moreover, Layer 9 is in immediate contact with the overlying sealing caprock; therefore, CO_2 behavior and fate in this specific layer will determine the long-term effectiveness and the security of the containment.[31,32]

In this study, we first simulated a base case by adopting a linear rate law (called "LIN law" hereafter)[33−35] for mineral dissolution and precipitation and by using the temperature, pressure, and mineralogy reported for Layer 9. Then, the Alekseyev et al.[16] type rate law (called "Alex law" hereafter) for feldspar dissolution and Burton−Cabrera−Frank (BCF) formulation[36] for secondary mineral precipitation were tested to investigate the effects of rate law uncertainties on the fate of injected CO_2. In addition, the effects of dissolution rate law uncertainties of silicate minerals other than feldspars were assessed on the basis of the above results.

Cases with a range of groundwater flow velocities (Darcy velocity from 0 to ~0.1 m/yr at 5000 m) were designed in order to explore the influences of regional groundwater flow on long-term CO_2 fate. Note that the purpose of our study is not to reproduce multiphase flow phenomenon of the long-term disposal of CO_2 in the Utsira Sand accurately but to explore the general effects of rate laws and regional groundwater flow on long-term CO_2 fate in the sandy aquifer resembling the uppermost layer (Layer 9) in the Utsira Sand.

2. SITE DESCRIPTION

The Utsira Sand extends along the UK/Norwegian median line for more than 450 km north−south and 75−130 km east−west (Figure 1a). The Utsira Sand has an average porosity of 35% and a permeability range of 1−5 Darcy, and it has a thickness ranging between 200 and 300 m with the top of the formation at about 800−1000 m below sea level at the injection point.[37−39] The injection point (Figure 1b) is located at 1012 m below the mean sea level.[40]

We chose Sleipner as our field site because of the availability of comprehensive data, including seismic and well log data. Up to 300 testing wells have been drilled, among which 30 wells are within 20 km of the injection site. Information collected from the wells includes lists of formation top, geophysical logs, reservoir core material, selected cuttings of caprock and reservoir rocks, and reservoir pressure measurements.[41] Baseline time-lapse 3D seismic data was acquired in 1994, prior to the injection. Repeat surveys were conducted in 1999, 2001, 2002, 2004, 2006, and 2008, with the latter two being augmented by a high-resolution 2D seismic and seabed imaging survey.[42] Nine CO_2 accumulation horizons are identified through seismic data. The topography (lateral extent, continuity, etc.) of each horizon is markedly different. However, only the uppermost CO_2 plume in Layer 9 (Figure

DOI: 10.1021/acs.energyfuels.5b02556
Energy Fuels 2016, 30, 4159−4180

Table 1. Hydrogeologic Parameters for Layer 9

parameters	adopted values	references
permeability (m^2)	2×10^{-12}	Singh et al.[39]
porosity	0.35	Singh et al.[39]
thickness (m)	10	
temperature (°C)	33.5	Boait et al.,[82] Cavanagh and Haszeldine[83]
pressure (kPa)	8300	Chadwick et al.,[40] Boait et al.[82]
CO_2 injection rate (kg/s)	3.5 (0−100 years)	
co-injected brine rate (kg/s)	1.0	
relative permeability		
liquid[84]		
$k_{rl} = \sqrt{S^*\{1 - (1 - [S^*]^{1/m})^m\}^2}$	$S^* = (S_l - S_{lr})/(1 - S_{lr})$	
S_l: liquid (water) saturation		
S_{lr}: irreducible water saturation	0.11	Singh et al.[39]
m: exponent	0.8	
gas[85]		
$k_{rg} = (1 - \hat{S})^2(1 - \hat{S}^2)$	$\hat{S} = \frac{(S_l - S_{lr})}{(1 - S_{lr} - S_{gr})}$	
S_g: gas saturation		
S_{gr}: residual gas saturation	0.21	Singh et al.[39]
capillary pressure		
Van Genuchten[84]		
$P_{cap} = -P_0([S^*]^{-1/m} - 1)^{1-m}$	$S^* = (S_l - S_{lr})/(1 - S_{lr})$	
S_{lr}: irreducible water saturation	0.11	
m: exponent	0.68	
P_0: strength coefficient (kPa)	2.5	Cavanagh[45]

1b) is clearly resolved based on the shallowest bright reflection in the seismic data, whereas the interpretation of lower CO_2 plumes is affected by the overlying bright seismic reflections. CO_2 accumulation over time has also been quantified in Layer 9,[43−45] and our current study only focuses on the CO_2 storage in this layer.

3. MODELING APPROACH

3.1. Conceptual Model. Layer 9 was assumed to be a homogeneous, isotropic sandstone formation at a depth of ∼820 m. The model thickness is 10 m to represent approximately the average CO_2 plume thickness in Layer 9 during 10 000 years simulation period. We derived this thickness based on a structural analysis by Chadwick and Noy,[46] who determined that the maximum thickness of CO_2 plume in Layer 9 in 2006 is ∼10 m. Starting in 1996, CO_2 separated from natural gas has been injected into the Utsira Sand at a rate of about 1 million metric tons of CO_2 per year.[29] Nine CO_2 accumulation horizons within the Utsira Sand are identified through seismic data. CO_2 started to spill into Layer 9 in 1999, but both the CO_2 spill life and the spill rate are uncertain because this project is still ongoing and has been going on for a relatively short duration to date. Hence, we assumed that the CO_2 spill life is 100 years, and the CO_2 spill rate into Layer 9 is 3.5 kg/s, which is the average spill rate from 1999 to 2009. The spill rate data from 1999 to 2009 is provided by Statoil. The effects of the CO_2 spill uncertainties, such as the CO_2 spill life and the spill rate into Layer 9, on the long-term CO_2 fate and whether and how these effects are affected by rate laws will be discussed in the succeeding text.

In this study, CO_2 sequestration was simplified as the 1D radial process of multiphase flow and reactive geochemical transport, due to the smaller thickness (10 m scale) compared to the potential lateral distance reached by CO_2 plume (km to tens of km scale). In the Base Case model, CO_2 was injected/spilled for 100 consecutive years without the coinjection of brine because the slow regional groundwater flow is inhibited by the increased pressure that results from CO_2 injection and is negligible during the injection period. After 100 years, the brine was injected at a rate of 1.0 kg/s (Darcy velocity ∼0.1 m/yr at 5000 m) without CO_2 until the end of simulation (10 000 years) to represent, approximately, the return of regional groundwater flow post-CO_2 spill. The typical range of maximum background Darcy velocity of the groundwater in deep sedimentary basin is 0.1−1 m/yr.[47,48] Therefore, the flow rate of 0.1 m/yr used here is on the high end. We also simulated a no-flow case. Hence, our simulations cover a range (0−0.1 m/yr) from the minimal to maximum flow rate. The model results with the flow rate of 0.1 m/yr approximately represent the maximum effect of the groundwater flow on long-term CO_2 sequestration.

3.2. Modeling Code. The simulations in the present study were conducted with the code TOUGHREACT/ECO2N which is developed for chemically reactive nonisothermal, density-dependent flows of multiphase fluids in porous and fractured media.[49,50] TOUGHREACT uses a rate expression from Lasaga et al.[51] for kinetic mineral reactions, and the rate constant is dependent on temperature and different mechanisms (such as neutral, acid, and base mechanisms). The aqueous complexation and dissolution/exsolution of CO_2 gas phase in the program is assumed to be instantaneous equilibrium.

3.3. Grid Design and Hydrogeologic Parameters. A radially symmetric grid model was set up in this study. The layer thickness is 10 m, and grid block sizes increase logarithmically from the wellbore at the origin to the outer

DOI: 10.1021/acs.energyfuels.5b02556
Energy Fuels 2016, 30, 4159−4180

Table 2. Initial Mineral Abundances (in Volume %) and Mineral Phases for Utsira Sandstone

minerals	Pearce et al.[54]	Chadwick et al.[55]	minerals used in this study	chemical composition	abundance
			Primary		
quartz	76.33	75	quartz	SiO_2	73.67
K-feldspar	6.93	13	K-feldspar	$KAlSi_3O_8$	13
plagioclase	3.01	3 (albite)	albite∼low	$NaAlSi_3O_8$	3
mica/illite	5.22	3	muscovite	$KAl_3Si_3O_{10}(OH)_2$	3
calcite	6.74	3	calcite	$CaCO_3$	6
chlorite	1.33		chlorite	$Mg_{2.5}Fe_{2.5}Al_2Si_3O_{10}(OH)_8$	1.33
aragonite		3	not used		
pyrite	0.05		not used		
ilmenite	0.12		not used		
apatite	0.02		not used		
zeolite	0.22		not used		
Ti oxides	0.03		not used		
			Secondary		
chalcedony			chalcedony	SiO_2	0.0
magnesite			magnesite	$MgCO_3$	0.0
dawsonite			dawsonite	$NaAlCO_3(OH)_2$	0.0
kaolinite			kaolinite	$Al_2Si_2O_5(OH)_4$	0.0
siderite			siderite	$FeCO_3$	0.0
dolomite-dis			dolomite-dis	$CaMg(CO_3)_2$	0.0
ankerite			ankerite	$CaFe_{0.7}Mg_{0.3}(CO_3)_2$	0.0

boundary of the model, which is approximately 15 000 m (far enough to avoid the disturbance to the boundary due to CO_2 injection). A constant pressure of 8300 kPa was assigned to Layer 9 initially, and reservoir pressure was allowed to build up because of CO_2 injection. The temperature of Layer 9 was 33.5 °C. Minor perturbations of the temperature may occur because of the injection,[52] but this was not considered in the simulations. The hydrological properties for Layer 9 are listed in Table 1.

3.4. Initial and Boundary Conditions. The boundary condition applied to our simulations for solving the reactive transport equations is a Dirichlet boundary condition. This Dirichlet boundary was implemented by assigning a large (infinite) volume to the boundary grid block.[53] Consequently, any influence from the influx becomes negligible compared to the large volume of the formation brine. The aqueous chemical composition of the boundary element, as well as its thermodynamic conditions, such as temperature and pressure, is therefore kept essentially unchanged from the original formation brine.[53] The sandstone layer is initially saturated with water, water saturation (S_l) = 1.

3.5. Mineral and Formation Water Composition. The mineralogical compositions for Utsira Sand (Sleipner site) used in the modeling simulations in the literature are mainly from two sources: Pearce et al.[54] and Chadwick et al.[55] However, the results from these two independent studies are similar (Table 2). We used the compositions based on Chadwick et al.[55] with minor modifications. Sandstone mineralogy from Chadwick et al.[55] was also adopted by the "Best Practice Manual, Saline Aquifer CO_2 Storage Project (SACS)".[41] The sandstone is composed mainly of quartz (73.67% of all minerals by volume), feldspar (13% K-feldspar and 3% of albite), calcite (6%), and small amounts of muscovite and chlorite. These minerals were allowed to precipitate if the solution was supersaturated with respect to them. In addition, following Audigane et al.[56] and Pham et al.,[57] aluminosilicate minerals chalcedony and kaolinite, and carbonate minerals magnesite, siderite, dawsonite, ankerite, and dolomite-dis (disordered dolomite) were selected as secondary minerals, which are the minerals that are formed/precipitated because of the CO_2−water−formaton rock interactions.

No data on the formation water composition was available at the Sleipner site. Previous studies used the Oseberg formation water as a representative for the Sleipner site.[6,56] Johnson et al.[58] slightly modified the chemical composition of the Oseberg formation water to align better with the mineralogy of the Utsira Sand formation. In this study, we adopted the formation water composition from Johnson et al. (Table 3).[58]

Table 3. Brine Composition in the Utsira Sandstone Formation

component	concentration (mol/kg H_2O)[a]
Na	0.4520
K	0.0053
Ca	0.00742
Mg	0.0181
Al	1.3×10^{-8}
Si	1.66×10^{-4}
Fe (total)	1.0×10^{-8} [b]
Cl	0.5213
C	0.00232
pH	7.2

[a]Johnson et al.[58] [b]Assumed value.

3.6. Thermodynamic Data. The thermodynamic data set was adopted from Xu et al.[59] The primary source for the equilibrium constants for the aqueous species and minerals used in this database originated from the EQ3/6 V7.2b database.[60] However, many substitutions and changes have been incorporated in response to more recent publications on the thermodynamic properties of several rock forming minerals and aqueous species. Among these are revisions to the feldspars by Arnorsson and Stefansson[61] and Stefansson and Arnórsson,[62] several clay minerals by Yates and Rosenberg,[63] chlorite by Xu et al.,[7] dawsonite by Ferrante et al.,[64] magnesite and

DOI: 10.1021/acs.energyfuels.5b02556
Energy Fuels 2016, 30, 4159−4180

Table 4. Adopted Kinetic Parameters for Minerals

mineral	log k_H (E_a)[a]	log k_{H_2O} (E_a)[b]	n[c]	reactive specific surface area[d]	rate law (Base Case)	rate law (Alex Case)	rate law (BCF Case)	rate law (Alex+BCF Case)
calcite	equilibrium	equilibrium			equilibrium	equilibrium	equilibrium	equilibrium
quartz		−13.99 (87.6)		9.8	LIN	LIN	dissolution: LIN; precipitation BCF	dissolution: LIN; precipitation BCF
K-feldspar	−10.06 (51.7)	−12.41 (38.0)	0.5	9.8	LIN	dissolution: Alex; precipitation: LIN	dissolution: LIN; precipitation BCF	dissolution: Alex; precipitation BCF
albite~low	−10.16 (65.0)	−12.56 (69.8)	0.457	9.8	LIN	dissolution: Alex; precipitation: LIN	dissolution: LIN; precipitation BCF	dissolution: Alex; precipitation BCF
muscovite	−11.85 (22.0)	−13.55 (22.0)	0.37	151.6	LIN	LIN	dissolution: LIN; precipitation BCF	dissolution: LIN; precipitation BCF
chlorite	−11.11 (88.0)	−12.52 (88.0)	0.5	9.8	LIN	LIN	dissolution: LIN; precipitation BCF	dissolution: LIN; precipitation BCF
chalcedony		−9.42 (49.8)[f]		9.8	LIN	LIN	dissolution: LIN; precipitation BCF	dissolution: LIN; precipitation BCF
kaolinite	−11.31 (65.9)	−13.18 (22.2)	0.777	151.6	LIN	LIN	dissolution: LIN; precipitation BCF	dissolution: LIN; precipitation BCF
magnesite	−6.38 (14.4)	−9.34 (23.5)	1.0	9.8	LIN	LIN	dissolution: LIN; precipitation BCF	dissolution: LIN; precipitation BCF
siderite	same as dolomite	−8.9 (62.76)[e]	same as dolomite	9.8	LIN	LIN	dissolution: LIN; precipitation BCF	dissolution: LIN; precipitation BCF
dawsonite	same as dolomite	same as siderite	same as dolomite	9.8	LIN	LIN	dissolution: LIN; precipitation BCF	dissolution: LIN; precipitation BCF
ankerite	same as dolomite	same as siderite	same as dolomite	9.8	LIN	LIN	dissolution: LIN; precipitation BCF	dissolution: LIN; precipitation BCF
dolomite-dis	−3.19 (36.1)	−7.53 (52.2)	0.5	9.8	LIN	LIN	dissolution: LIN; precipitation BCF	dissolution: LIN; precipitation BCF

[a]Log kinetic rate constant k_H (mol/m^2/s) at 25 °C and activation energy E_a (kJ/mol) for acid mechanism from Palandri and Kharaka.[69] [b]Log kinetic rate constant k_{H_2O} (mol/m^2/s) at 25 °C and activation energy E_a (kJ/mol) for neutral mechanism from Palandri and Kharaka.[69] [c]Power term n with respect to H^+ from Palandri and Kharaka.[69] [d]Reactive specific surface area (cm^2/g) based on Sonnenthal and Spycher,[72] which was reduced by 1 order of magnitude. [e]From Steefel.[70] [f]Data for chalcedony precipitation but the dissolution kinetics data were assumed to be the same as those for quartz.

dolomite by Rock et al.,[65] siderite by Preis and Gamsjager,[66] ankerite by Xu et al.,[49] and SiO_2(aq) by Rimstidt.[67]

3.7. Kinetics of Mineral Reaction. *3.7.1. Rate Law.* We have described the rate law uncertainties in detail in another publication.[25] In the present study, we employed the three different rate laws listed below to explore the effect of rate law uncertainties on long-term CO_2 fate in a sandy aquifer resembling the uppermost layer in the Utsira Sand, Sleipner: (1) Traditional linear rate law, LIN law,[33,34] used for mineral dissolution and precipitation

$$\frac{r}{S} = \pm k f(\Delta G_r) = \pm k\left[1 - \exp\left(\frac{\Delta G_r}{RT}\right)\right] \quad (1)$$

where r denotes the dissolution/precipitation rate in mol/kg H_2O/s, S is the reactive surface area per kg H_2O, k is the temperature-dependent rate constant (mol/m^2/s), $f(\Delta G_r)$ is the rate dependence on Gibbs free energy of the reaction ΔG_r, R is the universal gas constant, and T is the absolute temperature. (2) Nonlinear Alex law,[16] used for mineral dissolution only

$$\frac{r}{S} = \pm k f(\Delta G_r) = \pm k\left|1 - \left(\frac{Q}{K}\right)^p\right|^q \quad (2)$$

where Q is the activity quotient, K is the equilibrium constant, and p and q are fitting parameters. (3) Nonlinear BCF law,[36] used for mineral precipitation only

$$\frac{r}{S} = \pm k f(\Delta G_r) = \pm k\left[\exp\left(\frac{\Delta G_r}{RT}\right) - 1\right]^2 \quad (3)$$

We first constructed four scenarios, Base Case, Alex Case, BCF Case, and Alex+BCF Case (Tables 4 and 6), to explore whether uncertainties of the feldspar dissolution and secondary mineral precipitation rate laws have a large influence on CO_2 sequestration and how they affect the partitioning of injected CO_2 into different trapping mechanisms. In these scenarios, the permutation and combination of a nonlinear Alex law for feldspar dissolution, a nonlinear BCF formulation for secondary mineral precipitation, and a LIN rate law for dissolution and precipitation reactions was conducted. The details of the different scenarios simulation in this study are shown in Table 4. Because silicate alteration dominates the long-term geochemical interactions during CO_2 sequestration,[6,9,56,68] the effects of dissolution rate law uncertainties of silicate minerals other than feldspars were also assessed on the basis of the above results.

3.7.2. Rate Constant. Both the neutral mechanism and acid mechanism were taken into account to calculate the rate constant k in eq 1 because dissolution and precipitation are often catalyzed by H^+ (acid mechanism) in an acid environment such as CO_2 sequestration in saline aquifer. The general form of k including acid, base, and neutral mechanisms is stated in detail in eq B.11 of Xu et al.[49]

Calcite was assumed to be at equilibrium because its reaction rate is rapid compared to silicate minerals. The acid mechanism was taken into consideration only for mineral dissolution reactions for each mineral controlled by kinetics in our simulations. Precipitation reactions only employed a neutral pH mechanism because of the lack of precipitation rate data at different pH levels for most minerals. The kinetic parameters (the rate constants and the apparent activation energy)

DOI: 10.1021/acs.energyfuels.5b02556
Energy Fuels 2016, 30, 4159−4180

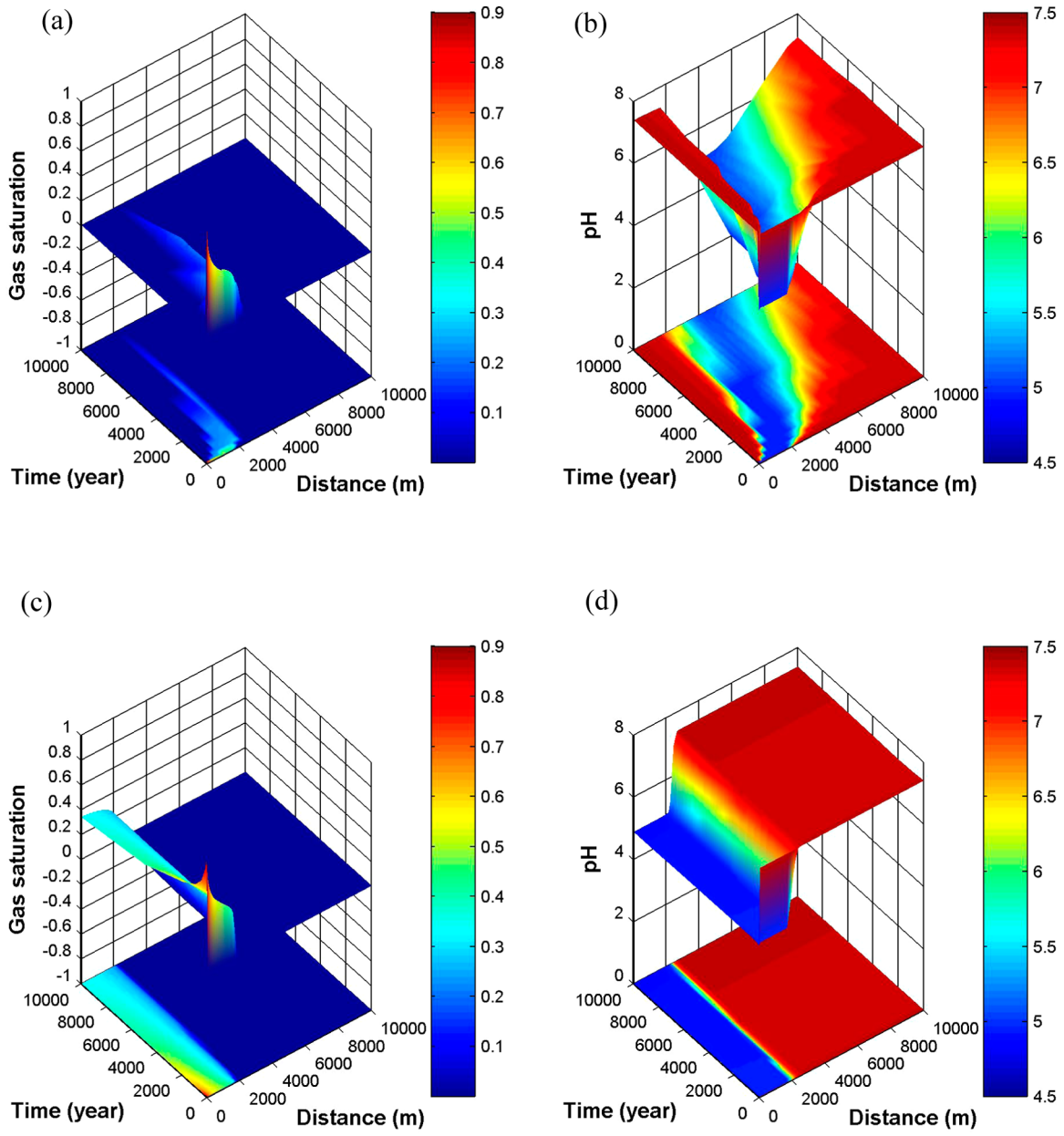

Figure 2. Temporal and spatial evolution of the gas saturation (S_g) and pH. (a) S_g for Base Case; (b) pH for Base Case; (c) S_g for "Test—no water flow A"; (d) pH for "Test—no water flow A". The color bars and bottom parts in a—d represent the value of S_g (or pH) and the plane projection of 3D figure, respectively.

employed here were taken directly from the literature[69,70] or set to the minerals with known kinetic properties (Table 4).

3.7.3. Reactive Specific Surface Area. The reactive specific surface area in natural geologic media, especially for multi-mineral systems, is not quantitatively understood at present. Generally, a specific surface area calculated from grain size may be a poor estimate of the hydrologically accessible mineral surface area because of many factors, such as coating and water flow channeling.[71] Reactive specific surface areas employed here were based on Sonnenthal and Spycher,[72] who calculated the reactive specific surface area assuming a cubic array of truncated spheres that make up the framework of the rock. However, the data of Sonnenthal and Spycher[72] were arbitrarily reduced by 1 order of magnitude in the present simulations to account for effects such as coating and water flow channeling. The reactive specific surface areas used in the present study (Table 4) are comparable with those used in Xu et al.[7] and Audigane et al.[56]

4. RESULTS

In this section, we focus only the results from the Base, Alex, BCF, and Alex+BCF Cases to investigate the impact of rate laws on long-term CO_2 sequestration.

4.1. CO_2 Gas Saturation. Figure 2a demonstrates the migration of the supercritical CO_2, denoted with the term "gas" hereafter, in the Base Case in a 3D view and its 2D projection view. In the Base Case, during the first 100 years of injection/spill, the CO_2(g) plume front migrates forward to ~2000 m, driven primarily by the pressure gradient that results from CO_2 injection. This pressure gradient gradually dissipates when the injection ceases, resulting in only ~600 m outward movement in the next thousands of years. In the meantime, the fresh brine

DOI: 10.1021/acs.energyfuels.5b02556
Energy Fuels 2016, 30, 4159−4180

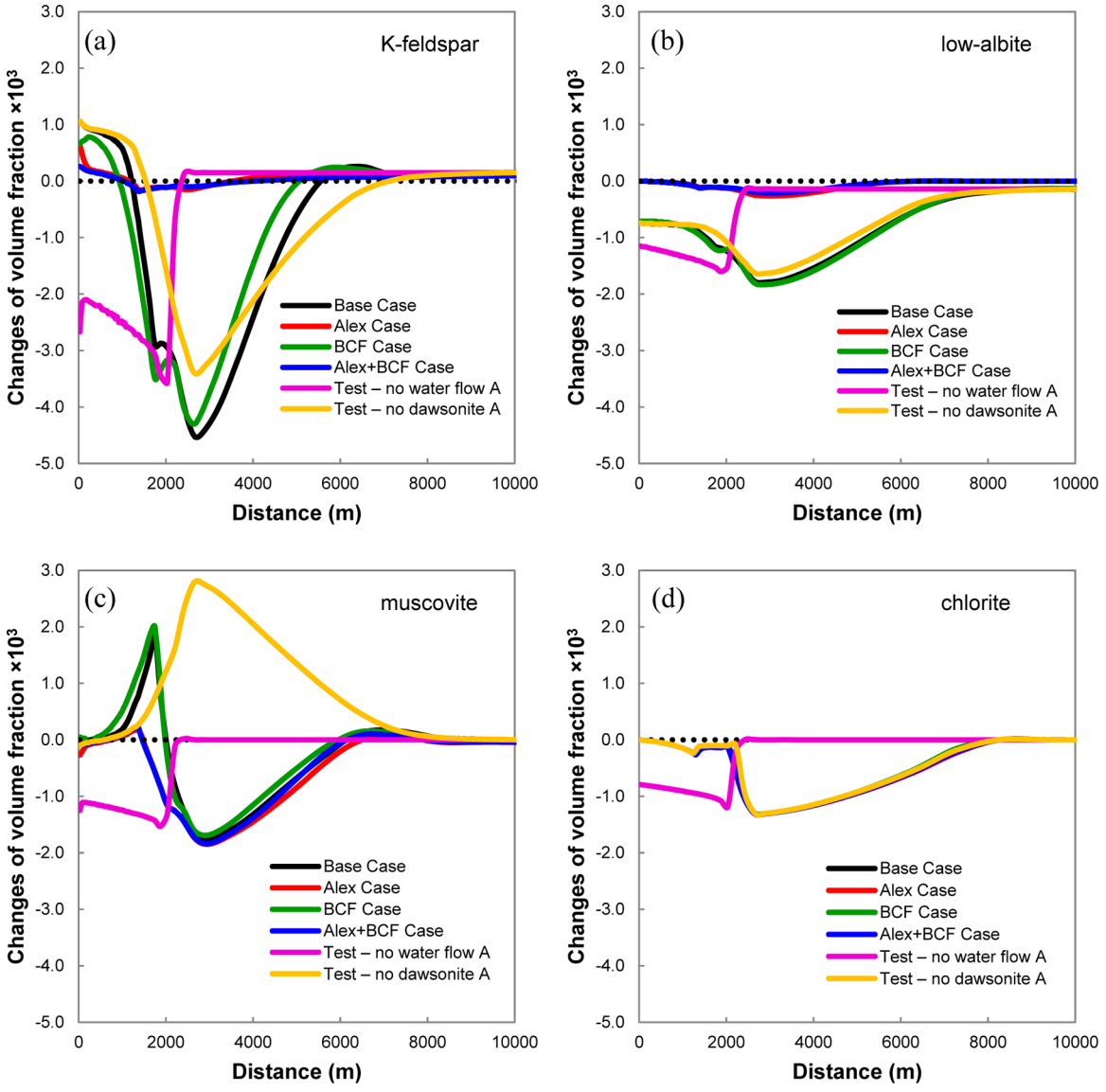

Figure 3. Volume fraction changes (VFC) of major silicate minerals at year 10 000. The black dotted line represents the zero value (no change). Positive values represent precipitation (increase of volume fraction), whereas negative values represent dissolution (decrease of volume fraction). (a) K-feldspar; (b) low-albite; (c) muscovite; and (d) chlorite.

invades back into pores occupied by the gas phase (imbibition process), and the gas saturation (S_g) is reduced, approaching the residual gas saturation (0.21).

The fresh brine from regional groundwater continuously dissolves CO_2 at the tail of CO_2 plume, generating $CO_{2,aq}$, $HCO_{3,aq}^{-}$, and $CO_{3,aq}^{2-}$, which are transported downstream by convection, diffusion, and dispersion. The concentration of $CO_{2,aq}$ is 1.19 mol/kg H_2O, which is comparable with that calculated by Audigane et al.[56] (~1.16 mol/kg H_2O) for Sleipner CO_2 sequestration. CO_2 dissolved into fresh brine causes the tail of CO_2 plume to move downstream with time and the size of the plume to shrink. At year 5000, the tail of CO_2 plume migrates to 1900 m in the Base Case (Figure 2a). At year 7000, the CO_2 in the gas phase dissolves into brine and transforms into carbonate minerals completely, and the S_g decreases from the initial value of 0.9–0.

The dissolved CO_2 distributes from ~1700 to 9000 m in the Base Case at year 10 000 because of the influence of regional groundwater flow. The maximum $CO_{2,aq}$ concentration at year 10 000 is ~0.8 mol/kg H_2O, which is slightly less than the concentration in equilibrium with CO_2 gas phase (~1.19 mol/kg H_2O). The reduction of $CO_{2,aq}$ concentration is primarily controlled by the dispersion process not by the slow mineral reactions.

Simulation results (not shown) indicate that changing the feldspar dissolution rate law (Base Case vs Alex Case; BCF Case vs Alex+BCF Case) or mineral precipitation rate law (Base Case vs BCF Case; Alex Case vs Alex+BCF Case) has insignificant effects on the evolution pattern of S_g. This is because the continuous dissolution of CO_2 caused by the groundwater flow is the main controller for the CO_2 gas saturation, not the slow mineral reactions. Therefore, the evolution of S_g is primarily controlled by the regional groundwater flow. Changing the rate laws has negligible effects on S_g evolution.

4.2. pH Evolution. In the Base Case, during the first 100 years of injection, the migration of the low pH zone is primarily controlled by the CO_2 plume and extends to ~2500 m at year

DOI: 10.1021/acs.energyfuels.5b02556
Energy Fuels 2016, 30, 4159–4180

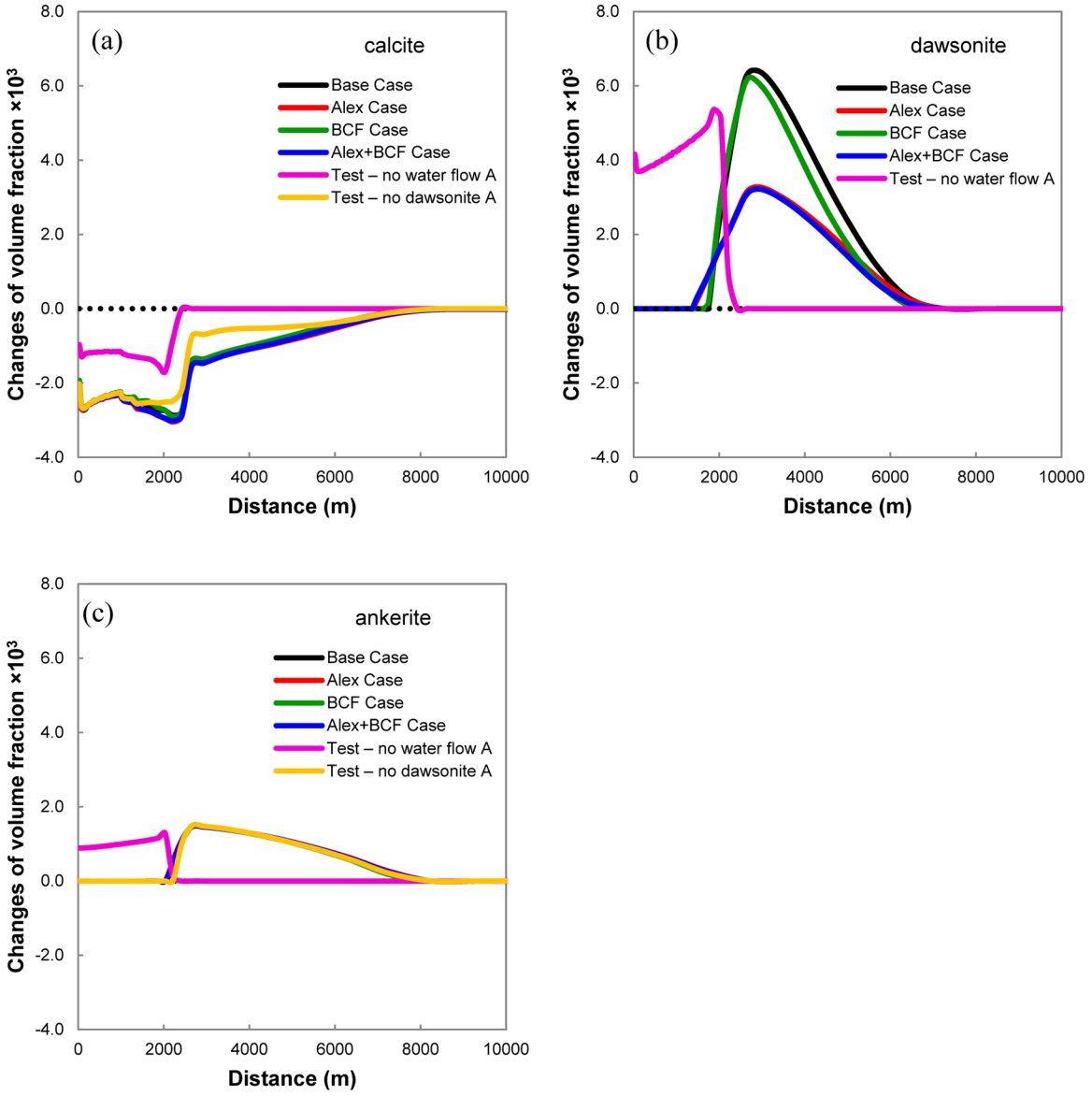

Figure 4. Volume fraction changes (VFC) of major carbonate minerals at year 10 000. The black dotted line represents the zero value. Positive values represent the precipitation, whereas negative values represent the dissolution. (a) Calcite; (b) dawsonite; and (c) ankerite.

100 (Figure 2b). However, in the following thousands of years, the transport of H^+ is primarily dominated by the regional groundwater flow, which drives the low pH front to ~9000 m at the end of simulation. The left boundary of the low pH zone is approximately consistent with the tail of CO_2 plume because of the CO_2 dissolution reaction, and it migrates to ~2000 m at year 5000. The lowest pH remains at ~4.9, similar to the value of 5.13 in Audigane et al.,[56] and is due to the buffering effects of calcite.

Calculated results (not shown) indicate that changing the feldspar dissolution rate law or mineral precipitation rate law does not have significant effects on the evolution of pH pattern. This is because pH is buffered by calcite and is not markedly influenced by the slow mineral reactions that are controlled by the kinetics. Therefore, rate laws have little effects on the evolution pattern of pH.

4.3. Evolution of Dominant Minerals. For the Base, Alex, BCF, and Alex+BCF Cases, the main reactive minerals during simulations are low-albite, K-feldspar, chlorite, calcite, muscovite, ankerite, dawsonite, and chalcedony. Both ankerite and dawsonite are the primary contributors for mineral trapping, whereas the dissolution of low-albite, K-feldspar, chlorite, calcite, and muscovite supplies relevant materials for carbonate precipitation. The coupling relationships among the reactive minerals are listed below (eq 4–7). Figures 3 and 4 show the volume fraction changes (VFC) of main reactive minerals (VFC = current VF − initial VF and VF = (volume of mineral of interest)/(total volume of the medium including the pores)). Positive values for VFC mean mineral precipitation and negative values represent dissolution.

$$\underset{}{CO_2(aq)} + H_2O + \underset{\text{albite}}{NaAlSi_3O_8} \rightarrow \underset{\text{chalcedony}}{3SiO_2} + \underset{\text{dawsonite}}{NaAlCO_3(OH)_2} \quad (4)$$

$$Na^+ + CO_2(aq) + H_2O + \underset{\text{K-feldspar}}{KAlSi_3O_8} \rightarrow K^+ + \underset{\text{chalcedony}}{3SiO_2} + \underset{\text{dawsonite}}{NaAlCO_3(OH)_2} \quad (5)$$

DOI: 10.1021/acs.energyfuels.5b02556
Energy Fuels 2016, 30, 4159–4180

$$3Na^+ + 3CO_2(aq) + 3H_2O + \underset{\text{muscovite}}{KAl_3Si_3O_{10}(OH)_2} \rightarrow 2H^+ + K^+ + \underset{\text{chalcedony}}{3SiO_2} + \underset{\text{dawsonite}}{3NaAlCO_3(OH)_2} \quad (6)$$

$$1.4Na^+ + 0.6H^+ + 3.9CO_2(aq) + \underset{\text{chlorite}}{0.7Mg_{2.5}Fe_{2.5}Al_2Si_3O_{10}(OH)_8} + \underset{\text{calcite}}{2.5CaCO_3} \rightarrow Mg^{2+} + 1.7H_2O + \underset{\text{chalcedony}}{2.1SiO_2} + \underset{\text{dawsonite}}{1.4NaAlCO_3(OH)_2} + \underset{\text{ankerite}}{2.5CaFe_{0.7}Mg_{0.3}(CO_3)_2} \quad (7)$$

4.3.1. Silicate Minerals. 4.3.1.1. Feldspar. The acidification of the brine due to the invasion of CO_2 leads to the dissolution of primary minerals K-feldspar, low-albite, and muscovite (Figure 3), which release the Na, Al, and Si into the brine. Because of the increased concentrations of Na, Al, and Si, the solution becomes supersaturated with respect to the secondary minerals, dawsonite and chalcedony, which start to precipitate (Figure 4). K-feldspar dissolution rate is fastest among K-feldspar, low-albite, and muscovite because it has a higher rate constant and initial surface area due to its high mineral abundance (13%, mineral abundance defined as the volume of the mineral of interest divided by the volume of the solid; Tables 2 and 4). At 2000 m and year 5000, the dissolution rate of K-feldspar is 6.3×10^{-13} mol/kg H_2O/s in the Base Case, whereas the values for low-albite and muscovite are 1.9×10^{-13} mol/kg H_2O/s and 1.4×10^{-13} mol/kg H_2O/s, which are 30% and 22% of K-feldspar dissolution rate, respectively. As a result, K-feldspar is the main source of Al for dawsonite. Muscovite is the second Al source because the stoichiometric coefficient of Al in the chemical formula of muscovite is three times that of low-albite. The slower dissolution rate of low-albite, as compared to that of K-feldspar, is caused by the smaller reactive surface area due to the lower initial mineral abundance (3%), which is ~23% of K-feldspar's value.

The coupling between K-feldspar and dawsonite/chalcedony (eq 5) results in the continuous dissolution of K-feldspar. In the Base Case, the minimum VFC of K-feldspar in the acidic region affected by the CO_2 invasion is -4.5 $\times 10^{-3}$ at year 10 000 (Figure 3a). Because the solution is supersaturated with respect to K-feldspar (saturation index (SI) = 0.1) in fresh brine, K-feldspar starts to precipitate near the injection well when the regional groundwater invades back into the pores after 100 years. The maximum VFC of K-feldspar near the injection well at year 10 000 is 1.0×10^{-3} in the Base Case.

The coupling between low-albite and dawsonite/chalcedony (eq 4) results in the continuous dissolution of low-albite. In the Base Case, the minimum VFC of low-albite in the acidic region at year 10 000 is -1.8×10^{-3} (Figure 3b). Different from K-feldspar, the solution is unsaturated with respect to low-albite in fresh brine. Low albite still dissolves near the injection well after the ceasing of CO_2 injection.

Figure 3a,b show that using Alex law in place of LIN law for feldspar dissolution (Base Case vs Alex Case; BCF Case vs Alex +BCF Case) significantly reduces the amount of K-feldspar and low-albite dissolution, while using different rate laws for mineral precipitation (Base Case vs BCF Case; Alex Case vs Alex+BCF Case) does not have a significant effect on the evolution of them. The minimum VFC of K-feldspar in the Base Case at year 10 000 is -4.5×10^{-3}, but in the Alex Case, it is only -1.85×10^{-3}, about 41% of that in the Base Case. The maximum dissolution rate of K-feldspar in the Base Case is 6.3×10^{-13} mol/kg H_2O/s, whereas in the Alex Case, it is only 0.45×10^{-13} mol/kg H_2O/s, ~7% of that in the Base Case. However, because of the high initial abundance (13%), the reactive surface area of K-feldspar in both the Base and Alex Cases remains at ~0.6 m^2/kg H_2O during the simulation. Therefore, in combination with the analysis of pH, different rate laws for feldspar dissolution have little effect on the reactive surface area and on the rate constant in eq 1, 2; rate laws affect the reaction rate and amount of K-feldspar dissolution mainly via rate–ΔG_r (or $f(\Delta G_r)$) relationships (Figure 7a,b).

Similar to K-feldspar, the minimum VFC of low-albite in the Base Case at year 10 000 is -1.8×10^{-3}, but in the Alex Case, it is only -0.3×10^{-3}, about 17% of that in Base Case. The maximum dissolution rate of low-albite in the Base Case is 1.9×10^{-13} mol/kg H_2O/s, whereas in the Alex Case, it is only 0.4×10^{-13} mol/kg H_2O/s, about 21% of that in the Base Case. The reactive surface area of low-albite varies only slightly, 0.13–0.14 m^2/kg H_2O, in both the Base and Alex Cases. Hence, as with K-feldspar, different rate laws for feldspar dissolution affect the reaction rate and dissolution amount of low-albite mainly through rate–ΔG_r relationships (Figure 7a,b).

4.3.1.2. Other Silicate Minerals. In the acidic region, muscovite dissolves and releases Al, which provides the material for dawsonite precipitation. The coupling between muscovite and dawsonite/chalcedony (eq 6) results in the continuous dissolution of muscovite. In the Base Case, the minimum VFC of muscovite at the acidic region is -1.8×10^{-3} at year 10 000 (Figure 3c). Similar to muscovite, because of the acidification of brine, chlorite dissolves and releases Fe and Mg, which results in the supersaturation and precipitation of ankerite. The precipitation of ankerite consumes Ca, which in turn promotes the dissolution of calcite to compensate for the consumption. The coupling between chlorite, calcite, and ankerite (eq 7) leads to the continuous dissolution of chlorite. In the Base Case, the minimum VFC of chlorite at the acidic region is -1.3×10^{-3} at year 10 000 (Figure 3d).

Muscovite and chlorite are more sensitive to the variation of pH than K-feldspar and low-albite because they need more H^+ per mole for dissolution. At the left boundary of acidic brine, muscovite and chlorite change from dissolution to precipitation (Figure 3c,d) when pH rises up to ~6.0. The precipitation of muscovite consumes K, Si, and Al, which are provided by the dissolution of K-feldspar and dawsonite. The precipitation of chlorite consumes Fe, Mg, and Al, leading to the dissolution of ankerite and dawsonite to compensate for the relevant solutes consumption. The conversion between dissolution and precipitation for muscovite caused by pH variation at the left boundary of acidic brine leads to a precipitation peak adjacent to a dissolution trough (Figure 3c). At year 10 000, the maximum VFC for the muscovite precipitation peak is 1.8×10^{-3} in the Base Case. The precipitation amount of chlorite at the left boundary of acidic brine is small and is barely enough to compensate the down-dip in the VFC lines due to previous dissolution of chlorite, resulting in a steeper reaction tail than the reaction front on the right-hand side (Figure 3d).

Figure 3c,d indicates that using Alex law in place of LIN law for feldspar dissolution (Base Case vs Alex Case; BCF Case vs Alex+BCF Case) does not have a significant effect on muscovite dissolution but does influence the precipitation of muscovite because Alex law reduces K-feldspar dissolution and the supply of K, Al, and Si for muscovite precipitation. Neither

DOI: 10.1021/acs.energyfuels.5b02556
Energy Fuels 2016, 30, 4159–4180

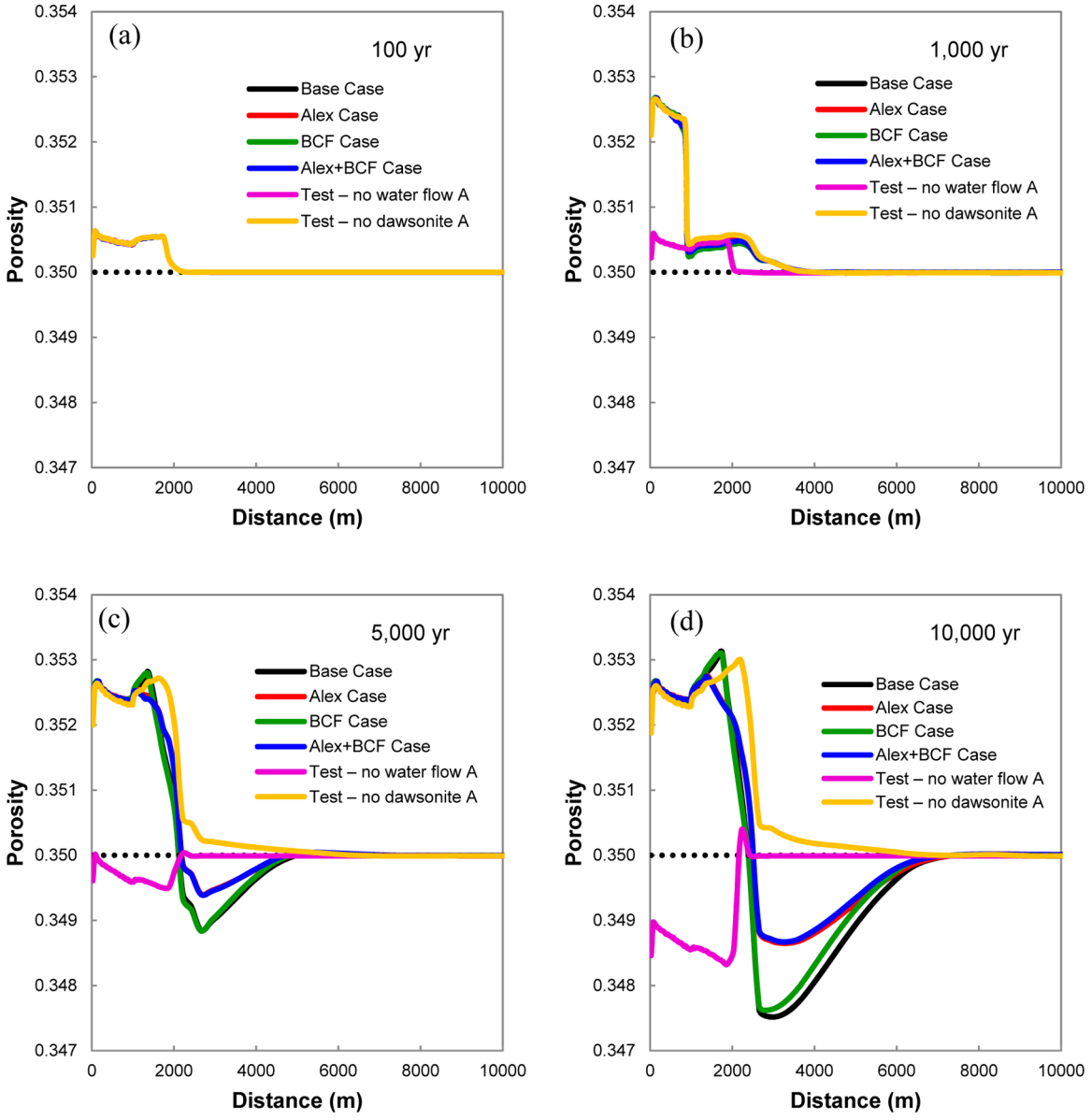

Figure 5. Temporal and spatial evolution of the porosity. Black dotted lines represent the initial porosity (0.35). (a) 100 years; (b) 1000 years; (c) 5000 years; and (d) 10 000 years.

changing rate laws for feldspar dissolution nor mineral precipitation impacts chlorite evolution.

4.3.2. Carbonate Minerals. 4.3.2.1. Calcite. During the first 100 years of CO_2 injection, part of the calcite dissolves in the CO_2 plume region because of the low pH caused by CO_2 dissolution. At year 100, VFC of calcite drops to -0.5×10^{-3} in the Base Case. In the following thousands of years, the fresh brine from regional groundwater flow is continuously acidized by CO_2 at the tail of CO_2 plume, leading to the continuous dissolution of calcite at the left boundary of the gas phase. In the Base Case, the VFC of calcite between 0 and 2700 m, the region swept by the tail of CO_2 plume, falls to ca. -2.5×10^{-3} at year 10 000 (Figure 4a). In the acidic region (Figure 2b), the solution is supersaturated with respect to ankerite. Ca consumption in ankerite precipitation is provided by the dissolution of calcite (eq 7). At year 10 000, between 2700 and 8300 m, where the calcite dissolution is primarily controlled by the precipitation of ankerite, the VFC of calcite in the Base Case drops to -1.4×10^{-3} at 2700 m and then gradually reaches zero downstream (Figure 4a). Figure 4a shows that neither changing rate laws for feldspar dissolution nor mineral precipitation has a significant impact on calcite evolution.

4.3.2.2. Dawsonite. In the acidic region (Figure 2b), the solution is supersaturated with respect to dawsonite due to the increased Na, Al, and Si concentrations caused by the dissolution of K-feldspar, low-albite, and muscovite, and dawsonite precipitates. In the Base Case, the maximum VFC of dawsonite in the acidic region is 6.3×10^{-3} at year 10 000 (Figure 4b). At the left boundary of acidic brine, muscovite and chlorite change from dissolution to precipitation (Figure 3c,d) when pH rises up to ~6.0. Their precipitation consumes Al, which leads to the continuous dissolution of dawsonite to compensate partly for the Al consumption. This causes previously precipitated dawsonite at the left boundary of the acidic region to be removed by subsequent dawsonite dissolution, resulting in a sharp reaction tail (Figure 4b).

Figure 4b indicates that using Alex law in place of LIN law for feldspar dissolution can reduce the amount of dawsonite

DOI: 10.1021/acs.energyfuels.5b02556
Energy Fuels 2016, 30, 4159−4180

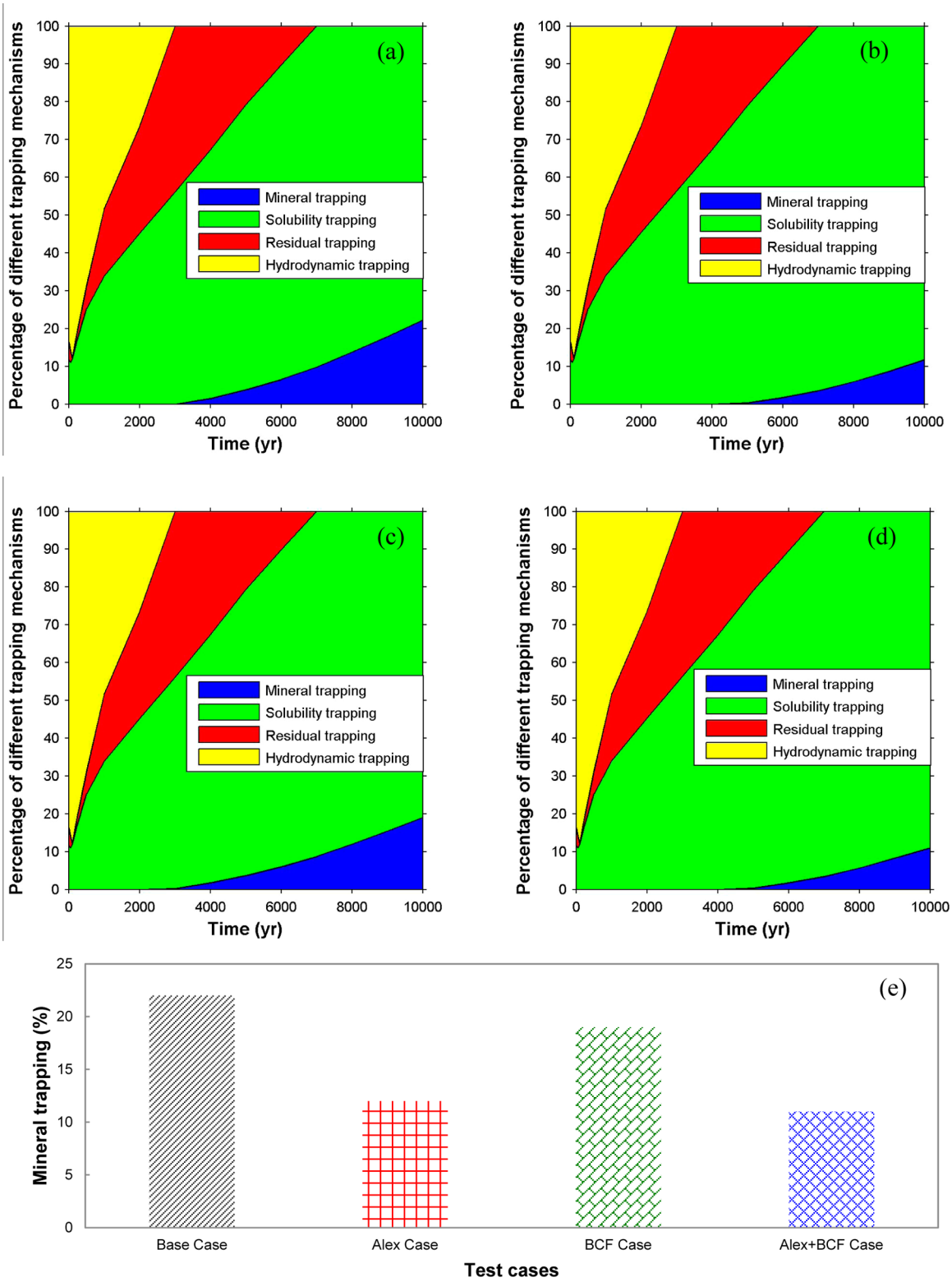

Figure 6. Percentage of different trapping mechanisms for the whole domain as a function of time. (a) Base Case; (b) Alex Case; (c) BCF Case; and (d) Alex+BCF Case. (e) Comparison of percentages of total injected CO_2 as mineral trapping at year 10 000 for the whole domain for Base, Alex, BCF, and Alex+BCF cases.

precipitation, but changing rate laws for mineral precipitation has an insignificant effect on dawsonite precipitation. At year 10 000, the largest amplitude of dawsonite VFC in the Base Case is 6.3×10^{-3}, whereas it is only 3.3×10^{-3} in the Alex Case, about 52% of that in the Base Case. This is because Alex law reduces the dissolution rate of K-feldspar and low-albite, whose dissolution offers Al and Na sources for dawsonite precipitation.

4.3.2.3. Ankerite. Because of the acidification of brine caused by CO_2 invasion, chlorite dissolves and releases Fe and Mg into

DOI: 10.1021/acs.energyfuels.5b02556
Energy Fuels 2016, 30, 4159−4180

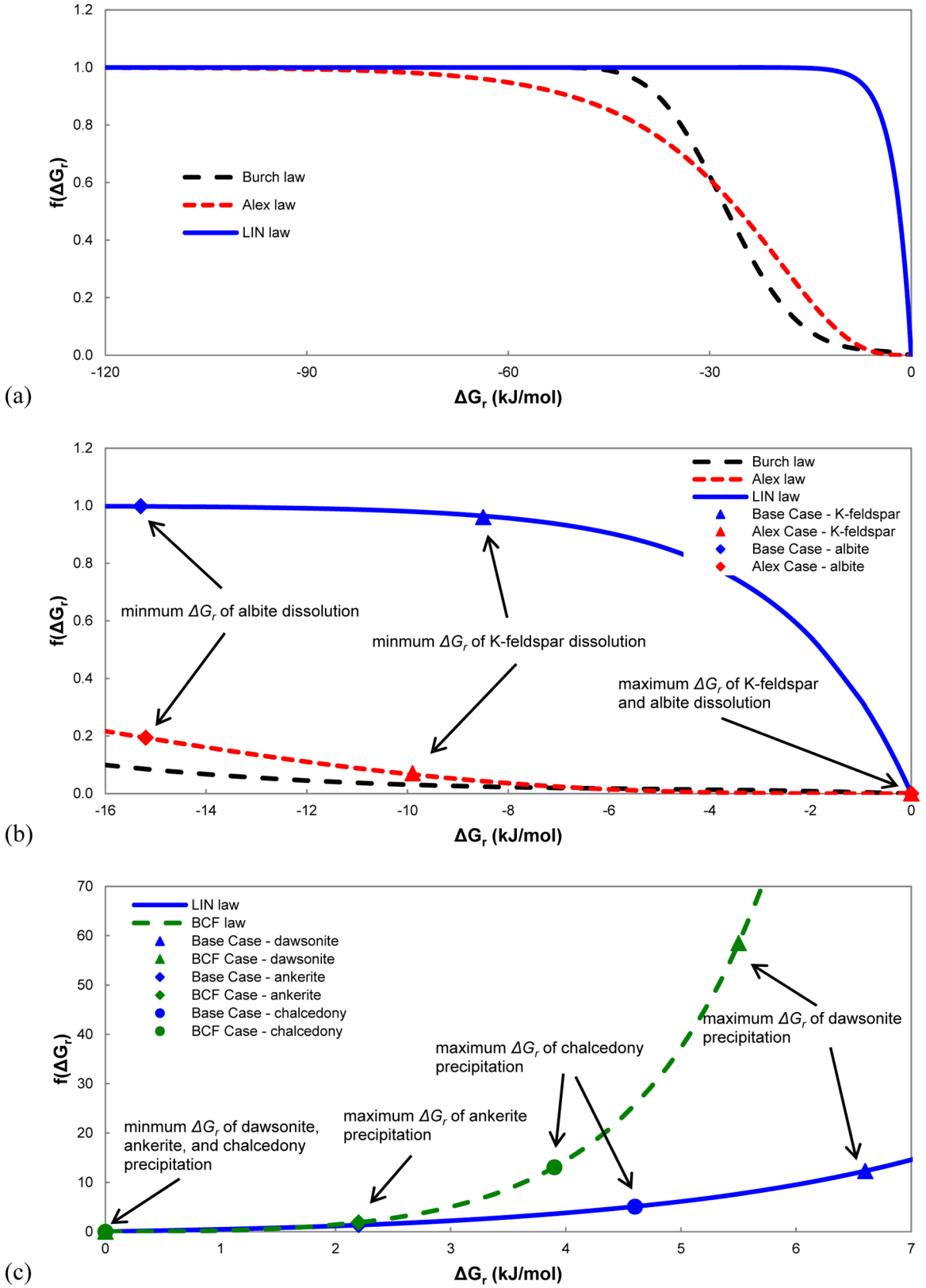

Figure 7. Relationship between $f(\Delta G_r)$ and ΔG_r for different rate laws. Scatter points are the related data extracted from the corresponding cases. (a) Comparison of feldspar dissolution rate laws. The curve of LIN rate law differs significantly from Burch and Alex laws in the transition and near equilibrium regions. Alex law is used to represent Burch law, as a compromise of the code capability. (b) Zoom in of a in the near equilibrium region. (c) Comparison of precipitation rate laws.

brine, leading to the supersaturation and precipitation of ankerite (eq 7). In the Base Case, the maximum VFC of ankerite at the acidic region is 1.5×10^{-3} at year 10 000 (Figure 4c). At the left boundary of acidic brine, chlorite changes from

DOI: 10.1021/acs.energyfuels.5b02556
Energy Fuels 2016, 30, 4159−4180

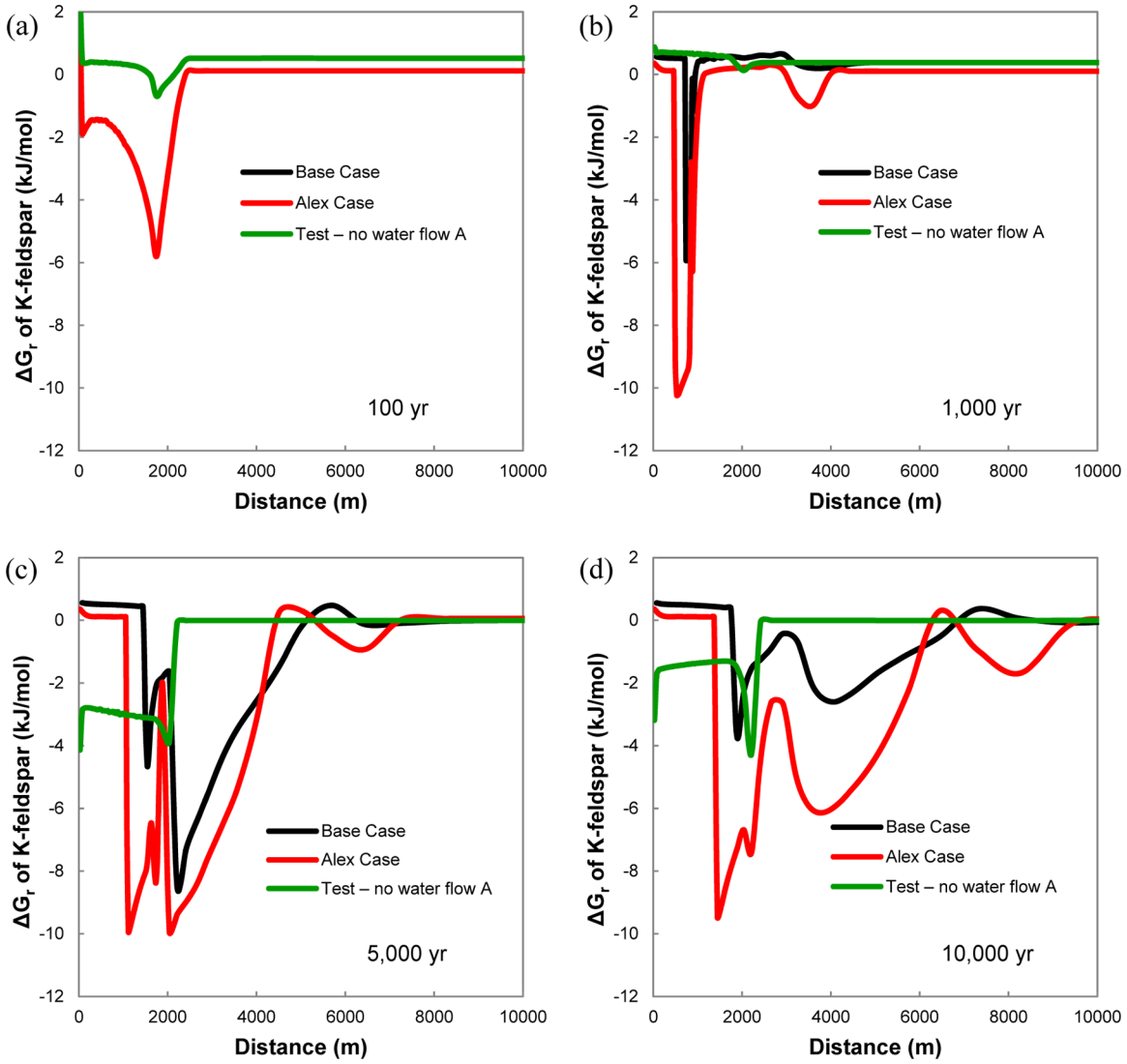

Figure 8. Temporal and spatial evolution of the ΔG_r for K-feldspar. (a) 100 years; (b) 1000 years; (c) 5000 years; and (d) 10 000 years.

dissolution to precipitation (Figure 3d) when pH rises up to ~6.0. Chlorite precipitation consumes Fe and Mg, which leads to the continuous dissolution of ankerite to compensate for the relevant consumption. This causes the previous ankerite precipitation at the left boundary of the acidic region to be removed by subsequent ankerite dissolution, resulting in a sharp reaction tail (Figure 4c). Figure 4c shows that neither changing rate laws for feldspar dissolution nor mineral precipitation has a significant impact on ankerite evolution because the dissolution rate law for chlorite has not been changed.

4.4. Porosity and Permeability. In the Base Case, the evolution of porosity upstream is primarily controlled by calcite dissolution, where the porosity increases from 0.35 to 0.3525 at year 10 000 (Figure 5). However, the porosity evolution downstream is mainly affected by the alteration of feldspar, muscovite, and chlorite, where the porosity decreases to 0.3475 at 3000 m and year 10 000 and the porosity gradually increases with distance after that. Overall, porosity changes are not significant during simulation time. The maximum porosity is 0.3525, only ~100.7% of the initial value, whereas the minimum value is 0.3476, ~99.3% of the initial value. In our simulation, permeability changes are evaluated from changes in porosity with the cubic law.[49] The variation of permeability is also not significant during simulation time. For example, the maximum permeability is 2.04×10^{-12} m^2, only ~102% of the initial permeability (2.0×10^{-12} m^2).

Figure 5 indicates that using Alex law in place of LIN law for feldspar dissolution can reduce the changes of porosity at the acidic region without the presence of CO_2 plume. In the Base Case, the minimum porosity is 0.3475, whereas it is only 0.3487 in the Alex Case.

4.5. Fate of the Injected CO_2. Different trapping mechanisms of CO_2 are closely related to underground CO_2 storage security, which can be approximated as the product of its capacity contribution (mass fraction), containment efficacy (vector and magnitude of gravitational mobility), and degrees of irreversibility.[73] Mineral trapping has been considered to be the safest mechanism in the long-term storage of CO_2.[4] In addition, the influence of the kinetic rate laws is likely to be the highest on mineral trapping compared to other trapping mechanisms. Hence, we focused mainly on the evolution of mineral trapping here.

Dawsonite and ankerite are the main carbonate mineral precipitations and contribute ~70 and ~30% to mineral trapping in the Base Case, respectively (Figure 6a). Using

DOI: 10.1021/acs.energyfuels.5b02556
Energy Fuels 2016, 30, 4159−4180

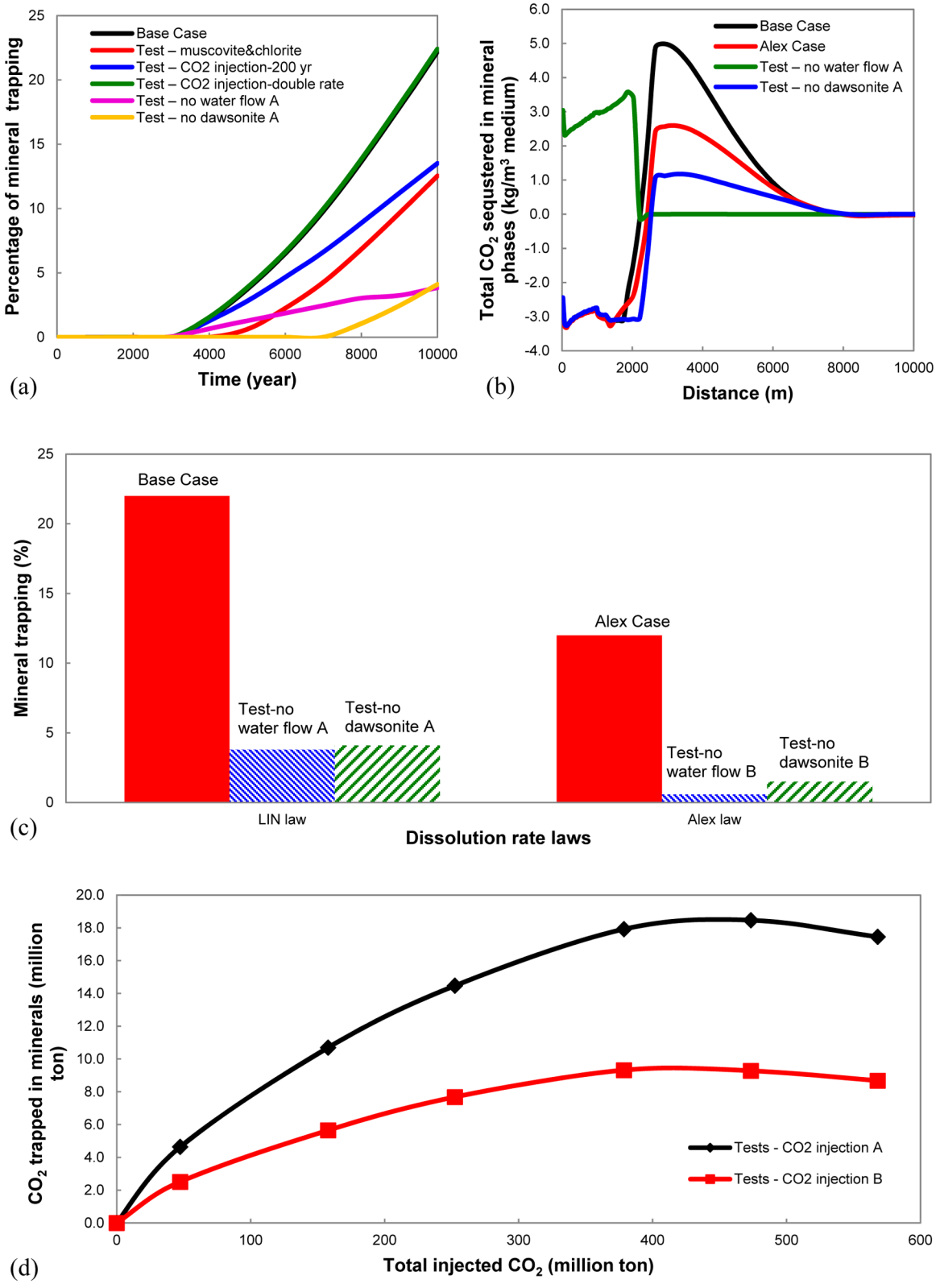

Figure 9. (a) Temporal evolution of mineral trapping (% of total CO_2 injected) for the whole domain. (b) Spatial evolution of mineral trapping (kg CO_2) at year 10 000 in the unit medium. (c) Percentage of mineral trapping at year 10 000 for the whole domain for Base Case, Alex Case, "Test−no water flow A", "Test−no water flow B", "Test−no dawsonite A", and "Test−no dawsonite B". (d) Relationships between mineral trapping (million tons CO_2) at year 10 000 for the whole domain and the total injected CO_2 for "Tests−CO_2 injection A" and "Tests−CO_2 injection B". Note the parameter settings of different cases are listed in Table 6.

Alex law in place of LIN law for feldspar dissolution reduces the fraction and delays the onset of mineral trapping for the whole domain, but changing rate laws for mineral precipitation (BCF law in place of LIN law) do not have a significant impact on

DOI: 10.1021/acs.energyfuels.5b02556
Energy Fuels 2016, 30, 4159−4180

those results (Figure 6a−d). At year 10 000, the percentage of mineral trapping for the whole domain in the Base Case is 22%, whereas it is only 12% in the Alex Case, about 55% of that in the Base Case (Figure 6e). For the whole domain, the CO_2 starts to be sequestrated in carbonate minerals from year 3000 in the Base Case, whereas it begins at year 4000 year in the Alex Case, postponing for ∼1000 years (Figure 6a,b). The spatial distributions of mineral trapping are the same in both the Base and Alex Cases, mainly in the acidic region not swept by the tail of CO_2 plume (Figure 9b). This is because the dissolution of calcite, which releases carbon, is the main carbonate reaction in the region that is swept by the tail of gas phase. At year 10 000, the peak value of mineral trapping (kg CO_2) in the unit medium in the Base Case is ∼4.9 kg/m^3 medium, whereas the value for the Alex Case is only ∼2.6 kg/m^3 medium (Figure 9b).

5. DISCUSSION

The four main coupled reactions (eq 4−7) that the invasion of CO_2 causes determine the formation and evolution of secondary carbonate minerals as a source of mineral trapping. The coupling between mineral dissolution (e.g., feldspar) and secondary mineral precipitation has been studied extensively.[18,19,21−23,74,75] Zhu et al.[19] found that the ways that reactions are coupled primarily depends on rate laws and surface areas. Below, we discuss in detail how rate laws control mineral trapping through affecting the coupled reactions. In addition, we will discuss how uncertainty factors, such as the regional groundwater flow, CO_2 spill (such as spill rate and spill life into Layer 9), and dawsonite presence, influence long-term CO_2 fate and interact with rate laws.

5.1. Effect of Rate Laws on the Coupling and CO_2 Sequestration Safety. *5.1.1. Dissolution Rate Laws of Feldspars.* The Base and Alex Cases are chosen as representative for analyzing the effect of different dissolution rate laws of feldspars. For feldspars, we only discuss K-feldspar because it is the main reactive feldspar in the simulation (Figure 3) as a result of its high initial abundance (13%). The Base and Alex Cases used a linear and a nonlinear rate−ΔG_r (or $f(\Delta G_r)$) relationship (Figure 7a,b) for feldspar dissolution, respectively. Figure 8d shows that there are two major ΔG_r troughs for K-feldspar. The left one is caused by the precipitation of muscovite, and the right one is due to the acidification of brine. We focus on the effect of dissolution rate laws in the acidic region because reactions driven by the acidification of brine are dominant reactions during CO_2 sequestration and determine the evolution of mineral trapping.

In the acidic region caused by CO_2 invasion, the K-feldspar ΔG_r in both of the Base and Alex Cases ranges only between ca. −10 and ∼0 kJ/mol (Figure 8), belonging to the near-equilibrium region where the discrepancy of rates between LIN and Alex law is larger than the far-from-equilibrium region (Figure 7a). In this ΔG_r region, the slope of LIN law is ∼14 times that of Alex law. Therefore, $f(\Delta G_r)$ of K-feldspar in the Base Case is more sensitive to ΔG_r (or the acidification of brine) than in the Alex Case. Figure 7b shows that the maximum $f(\Delta G_r)$ of K-feldspar in the acidic region in the Base Case is 0.96, whereas it is only 0.07 in the Alex Case, ∼7% of that in the Base Case. The differences between the $f(\Delta G_r)$ of K-feldspar in Base and Alex Cases result in that the K-feldspar dissolution rate (a function of $f(\Delta G_r)$) simulated with LIN law is much faster. More carbonate mineral precipitates because of the coupling between K-feldspar dissolution and dawsonite/chalcedony precipitation (eq 5, Figure 6e). In summary, using LIN law in place of Alex law for K-feldspar dissolution promotes the K-feldspar dissolution and carbonate mineral precipitation (mineral trapping) through increasing sensitivity of the coupled reaction rate of K-feldspar and carbonate minerals to the acidification of brine (or ΔG_r).

5.1.2. Dissolution Rate Laws of Silicate Minerals. Zhang et al.[25] investigated the effect of different rate laws on CO_2 trapping in a sandy aquifer resembling the Mt. Simon formation in the U.S. Midwest, which covers most of Illinois, western Indiana, and western Kentucky at depths from close to the surface to over 4600 m. They found that using LIN law in place of Alex law for feldspar dissolution increases the sensitivity of the coupled reaction rate of K-feldspar and illite/quartz to the acidification of brine, leading to more K-feldspar dissolution. However, in Zhang et al.,[25] carbonate mineral precipitation and mineral trapping are facilitated indirectly by the increased pH due to K-feldspar dissolution, not directly by the coupling between K-feldspar and carbonate minerals as in the present study. Combining the finding of Zhang et al.[25] with those from the present study and extrapolating from feldspars to all soluble silicate minerals, we suggest that changing the dissolution rate laws of the main soluble silicate mineral can influence silicate reaction and mineral trapping by altering the sensitivity of the relevant coupled reaction rate to the acidification of brine. The steeper the slope of the rate−ΔG_r relationships, the more sensitive the coupled reaction rate and the mineral trapping are to the acidification of brine.

We designed a test case, "Test−muscovite and chlorite" (Table 6), with Alex law for muscovite and chlorite dissolution (others to be the same as the Base Case) to test this hypothesis. Experimental studies on rates−ΔG_r relationship for muscovite dissolution in acidic pH are scarce, especially at near-equilibrium regions. Zhang et al.[76] investigated the kinetic dissolution of chlorite (the chlorite sample was from Flagstaff Hill, California) at 100 °C with a pH ranging from 3.0 to 7.5 and found that the rate−ΔG_r relationship for chlorite is nonlinear. As a result, in "Test−muscovite and chlorite", p and q in eq 2 for muscovite were set to be the same as those for K-feldspar and low-albite in the Alex Case, which are 0.184 and 4.04, respectively, to represent approximately the uncertainties of rate−ΔG_r relationship for muscovite dissolution. For chlorite, p and q were set to be 0.0599 and 1.557, respectively, to fit the nonlinear rate−ΔG_r relationship for chlorite dissolution found by Zhang et al.[76] The results indicate that the maximum VFC of dawsonite and ankerite at year 10 000 decrease from 6.31 × 10^{-3} to 4.28 × 10^{-3} (∼32% reduction) and from 1.46 × 10^{-3} to 1.03 × 10^{-3} (∼29% reduction), when compared to the Base Case. The percentage of mineral trapping (including all carbonate minerals) at year 10 000 also decreases from 22 to 13% (Figure 9a). This, to some extent, supports the hypothesis that we suggested above. Thus, experimental and numerical studies for the kinetics of silicate minerals other than feldspars (e.g., muscovite, chlorite, kaolinite, etc.) under CO_2 storage conditions are urgently needed.

5.1.3. Precipitation Rate Laws. The main secondary minerals are dawsonite, ankerite, and chalcedony. The comparison of simulated results (Base Case vs BCF Case; Alex Case vs Alex+BCF Case) indicates that using different precipitation rate laws (the first or second order dependence of precipitation on ΔG_r (Figure 7c)) do not have obvious impact on the evolution of minerals (Figures 3 and 4) and on the percentages of mineral trapping for the whole domain at year

DOI: 10.1021/acs.energyfuels.5b02556
Energy Fuels 2016, 30, 4159−4180

10 000 (Figure 6e). Among the main coupled reactions (eq 4−7), the precipitation of secondary minerals (dawsonite, ankerite, and chalcedony) are faster reactions, whereas the dissolution of primary minerals (feldspar, muscovite, and chlorite) are slower reactions (Table 4). The later reactions are the rate limiting factors controlling the long-term evolution of the coupling. Therefore, changing rate laws for mineral precipitation do not have an obvious effect on the mineral evolution and the mineral trapping.

5.2. Regional Groundwater Flow. To date, although several researchers considered regional groundwater flow in the reactive transport modeling of the CO_2 sequestration in geologic formations,[25−28] they lacked the detailed quantitative analysis of its impact on the long-term fate of the injected CO_2. Hence, below we discuss the potential effect of the regional groundwater flow uncertainties on long-term CO_2 fate and whether and how rate laws influence the effect of regional groundwater flow.

First, we designed a test case, "Test−no water flow A" (Table 6), to investigate the effect of the regional groundwater flow, and this test case has no regional groundwater flow post-CO_2 spill and keeps all other parameters the same as the Base Case. With the consideration of regional groundwater flow, the fresh brine from upstream migrates into the simulated domain and is acidified by the CO_2 at the left boundary of CO_2 plume, resulting in the reaction system far from the equilibrium. Hence, more mineral reacts, and the porosity in the acidic region is smaller (Figures 3−5 and Table 5). For example, the minimum ΔG_r of the major feldspars, K-feldspar, in the acidic region is only ca. −4 kJ/mol in "Test−no water flow A", but it decreases to ca. −8.5 kJ/mol in the Base Case (Figure 8). The lower ΔG_r facilitates the dissolution of K-feldspar in the Base Case. Therefore, the minimum VFC of K-feldspar at year 10 000 is only -3.5×10^{-3} in "Test−no water flow A", whereas it is -4.5×10^{-3} in the Base Case, ∼1.3 times of that in "Test−no water flow A".

Table 5. Comparison of Simulated Results from the Base Case and the "Test−No Water Flow A" Case at Year 10 000

	Base Case	Test−no water flow A
maximum Sg	0.0	0.35
minimum pH	5.0	4.9
area of acidic brine (m^2)	270×10^6	15×10^6
mineral trapping	21.0%	3.8%
VFC of Major Silicate Minerals		
K-feldspar	-4.5×10^{-3}	-3.5×10^{-3}
low-albite	-1.8×10^{-3}	-1.6×10^{-3}
muscovite	-1.8×10^{-3}	-1.5×10^{-3}
chlorite	-1.3×10^{-3}	-1.2×10^{-3}
VFC of Major Carbonate Minerals		
calcite	-2.5×10^{-3}	-1.7×10^{-3}
dawsonite	6.3×10^{-3}	5.5×10^{-3}
ankerite	1.5×10^{-3}	1.3×10^{-3}

With the washout of the fresh brine from the upstream, the gas phase disappears completely at year 7000 in the Base Case, but a significant portion of injected CO_2 in "Test−no water flow A" still exists as gas phase at year 10 000 (Figure 2a, c; Table 5). This finding is consistent with most previous work that used a 10 000 year simulation period.[8,77−79] In the Base and "Test−no water flow A" cases, the lowest pH only slightly changes (∼4.9) because of the same buffer effects caused by calcite (Figure 2b,d; Table 5). The regional groundwater flow transports the dissolved CO_2 downstream by convection and dispersion, forming a larger area of the acidic brine where mineral trapping can occur. The coverage area of acidic brine in "Test−no water flow A" at year 10 000 is only $\sim 0.15 \times 10^8$ m^2, whereas it is $\sim 0.27 \times 10^9$ m^2 in the Base Case, ∼18 times of that in "Test−no water flow A" (Figure 2b,d, Table 5). The mineral trapping fraction at year 10 000 for the whole domain is smaller, ∼3.8%, in "Test−no water flow A", whereas it is larger, ∼22%, in the Base Case, ∼5.8 times of that in "Test−no water flow A" (Figure 9a). The increase of the acidic area is the major reason for the rise in the percentage of mineral trapping.

The mineral trapping fraction for the whole domain increases with time in both the Base and "Test−no water flow A" cases. At year 10 000, the peak value of mineral trapping (kg CO_2) in the unit medium in Base Case (∼4.9 kg/m^3 medium) is located near the right boundary of the CO_2 plume (∼2600 m). However, the mineral trapping in "Test−no water flow A" primarily occurs at the region (0−1900 m) covered by the CO_2 plume and the value is approximately constant (∼3.0 kg/m^3 medium, Figure 9b). The reason for the negative mineral trapping in the Base Case near the well (Figure 9b) is that the calcite dissolution due to continuous acidification of the fresh brine from the regional groundwater flow is the main reaction for carbonate minerals in that region.

Next, we designed a test case, "Test−no water flow B" (Table 6) to investigate whether and how rate laws influence the effect of regional groundwater flow on long-term CO_2 fate. This test case has no regional groundwater flow post-CO_2 spill and keeps all other parameters the same as the Alex Case. If using LIN law, then the regional groundwater flow increases the percentage of mineral trapping by 18.2%, comparing the Base Case with "Test−no water flow A". If using Alex law, then the percentage of mineral trapping only increases by 11.4%, comparing the Alex Case with "Test−no water flow B" (Figure 9c). This is because the fresh brine from upstream can maintain ΔG_r far from zero while the effect of ΔG_r on the reaction rate and mineral trapping is controlled by the rate laws. There is a positive correlation between the steepness of the slope of the rate−ΔG relationships and the enhancement effect of groundwater flow on the reaction rate and mineral trapping.

In addition, a test case, "Test−no water flow-time" (Table 6), with no regional groundwater flow and the simulation time extended to 6 million years (others to be the same as the Base Case) was conducted to investigate the mineral assemblage when the reactive system reaches equilibrium. After six million years, in the acidic region, low-albite, muscovite, and chlorite are completely dissolved, and the mineral assemblage is composed of quartz, K-feldspar, chalcedony, kaolinite, calcite, dawsonite, and ankerite. The main contributors for mineral trapping are still dawsonite and ankerite. The maximum mineral trapping (kg CO_2) in the unit medium in "Test−no water flow-time" is ∼19.6 kg/m^3 medium, ∼6.5 times that in "Test−no water flow A".

5.3. CO_2 Spill Uncertainties. Both the CO_2 spill duration and the spill rate are uncertain because the ongoing Sleipner project is of relatively short duration to date. First, we conducted two test cases, "Test−CO_2 injection-200 yr" and "Test−CO_2 injection-double rate" (Table 6), to analyze how the uncertainties of CO_2 spill rate and spill duration affect the fractions of mineral trapping: (1) "Test−CO_2 injection-200 yr": CO_2 spill duration extends to 200 years, with all other parameters remaining the same as the Base Case; (2) "Test−

DOI: 10.1021/acs.energyfuels.5b02556
Energy Fuels 2016, 30, 4159−4180

Table 6. List of the Setups for Cases Simulated in This Study

cases	parameters				
	simulation time	CO_2 injection	groundwater	rate law	minerals
Base Case	10 000 years	3.5 kg/s (100 years)	yes	dissolution: LIN; precipitation: LIN	
Alex Case	10 000 years	3.5 kg/s (100 years)	yes	dissolution: LIN (except K-feldspar and albite~low with Alex); precipitation: LIN	
BCF Case	10 000 years	3.5 kg/s (100 years)	yes	dissolution: LIN; precipitation: BCF	
Alex+BCF Case	10 000 years	3.5 kg/s (100 years)	yes	dissolution: LIN (except K-feldspar and albite~low with Alex); precipitation: BCF	
Test−no water flow A	10 000 years	3.5 kg/s (100 years)	no	dissolution: LIN; precipitation: LIN	
Test−no water flow B	10 000 years	3.5 kg/s (100 years)	no	dissolution: LIN (except K-feldspar and albite~low with Alex); precipitation: LIN	
Test−no water flow-time	6 million years	3.5 kg/s (100 years)	no	dissolution: LIN; precipitation: LIN	
Test−no dawsonite A	10 000 years	3.5 kg/s (100 years)	yes	dissolution: LIN; precipitation: LIN	no dawsonite
Test−no dawsonite B	10 000 years	3.5 kg/s (100 years)	yes	dissolution: LIN (except K-feldspar and albite~low with Alex); precipitation: LIN	no dawsonite
Test−muscovite and chlorite	10 000 years	3.5 kg/s (100 years)	yes	dissolution: LIN (except muscovite and chlorite with Alex); precipitation: LIN	
Test−CO_2 injection-200 yr	10 000 years	3.5 kg/s (200 years)	yes	dissolution: LIN; precipitation: LIN	
Test−CO_2 injection -double rate	10 000 years	7.0 kg/s (50 years)	yes	dissolution: LIN; precipitation: LIN	
Tests−CO_2 injection A	10 000 years	0−180 kg/s (100 years)	yes	dissolution: LIN; precipitation: LIN	
Tests−CO_2 injection B	10 000 years	0−180 kg/s (100 years)	yes	dissolution: LIN (except K-feldspar and albite~low with Alex); precipitation: LIN	

CO_2 injection-double rate": CO_2 spill rate doubles and CO_2 spill duration is reduced to a half, with other parameters remaining the same as the Base Case.

Doubling the CO_2 spill rate but reducing its spill duration in half has an insignificant impact on mineral trapping. At year 10 000, the mineral trapping fraction in "Test−CO_2 injection-double rate" is the same as that in the Base Case (~22%) (Figure 9a) because the total amount of CO_2 spilled does not change. Therefore, focusing on the CO_2 spill rate or spill duration separately for the long-term fate of the injected CO_2 is not of great significance, but analyzing from the perspective of the total amount of CO_2 spilled is needed. Simulation results indicate that the increase of the total CO_2 spilled can reduce the percentage of mineral trapping. The percentage of CO_2 trapped by carbonate mineral at year 10 000 in "Test−CO_2 injection-200 yr" decreases from 22 to 14%, compared to the Base Case (Figure 9a).

Second, we designed two test series, "Tests−CO_2 injection A" and "Tests−CO_2 injection B" (Table 6), to investigate how the total CO_2 spilled impacts the mass of CO_2 trapped in the minerals at year 10 000 for the whole domain and how the rate laws influence the estimation of mineral trapping capacity (million tons CO_2), which is inferred from the relationship between the mass of CO_2 trapped in the minerals and the total CO_2 spilled (Figure 9d). "Tests−CO_2 injection A": a series of cases, the same as Base Case (LIN law for feldspar dissolution) except using different CO_2 injection rates; "Tests−CO_2 injection B": a series of cases, the same as Alex Case (Alex law for feldspar dissolution) except using different CO_2 injection rates.

The results from "Tests−CO_2 injection A" indicate that the mineral trapping (million tons CO_2) at year 10 000 for the whole domain increases to ~18 million tons with increased CO_2 spill and then decreases (Figure 9d). The reason is that the area covered by the CO_2 gas phase increases initially with the CO_2 spill rising, which promotes the mineral reaction. However, after the whole domain is covered by the gas phase, the additional CO_2 spill drives out the brine (a medium for chemical reactions), leading to smaller amounts of minerals reacted. The peak value of the mineral trapping in Figure 9d is defined as the theoretical mineral trapping capacity, corresponding to the time when gas phase starts to escape to the space beyond the outer boundary. The theoretical mineral trapping capacity ignores some practical limitations (e.g., geology, engineering, legal, regulatory, and economic barriers). Comparing "Tests−CO_2 injection A" with 'Tests−CO_2 injection B", using Alex law for feldspar dissolution in place of LIN law decreases the relevant coupled reaction rate, which inhibits the effect of the total CO_2 spilled on the mass of CO_2 trapped in the minerals (Figure 9d). Hence, the theoretical mineral trapping capacity at year 10 000 reduces from ~18 million ton in "Tests−CO_2 injection A" to ~9 million ton in "Tests−CO_2 injection B" (50% reduction).

If scaling the mineral trapping capacity at year 10 000 for the simulated domain to the whole Utsira Sand and assuming only the effective porous volume within the traps of the Utsira Sand (6.6×10^8 m^3 estimated by Chadwick et al.[55]) available for mineral sequestration, then we estimated the total values of ~6 million tons (LIN law for feldspar dissolution) and ~3 million tons (Alex law for feldspar dissolution) mineral trapped CO_2, respectively. However, if assuming that the acidic brine can cover all the porosity in the Utsira Sand (6.0×10^{11} m^3 from Chadwick et al.[55]) and that the unit volume medium of Utsira Sand has the same mineral trapping potential as that in our simulation, then we obtained larger values of ~5000 million tons (LIN law for feldspar dissolution) and ~2500 million tons (Alex law for feldspar dissolution), respectively. The huge differences between the estimated mineral trapping capacities between the two scenarios call for further research on the reactive transport of the acidic brine under the practical reservoir conditions and the active CO_2 sequestration managements.

5.4. Dawsonite. Albite, K-feldspar, and muscovite commonly weather to form kaolinite not dawsonite. To justify the alteration reactions of feldspar and muscovite in eq 4−6 and to explain why clay mineral, chlorite, reacts in the current way with the products of ankerite and dawsonite (eq 7), we established equilibrium activity−activity diagram at 33.5 °C

DOI: 10.1021/acs.energyfuels.5b02556
Energy Fuels 2016, 30, 4159−4180

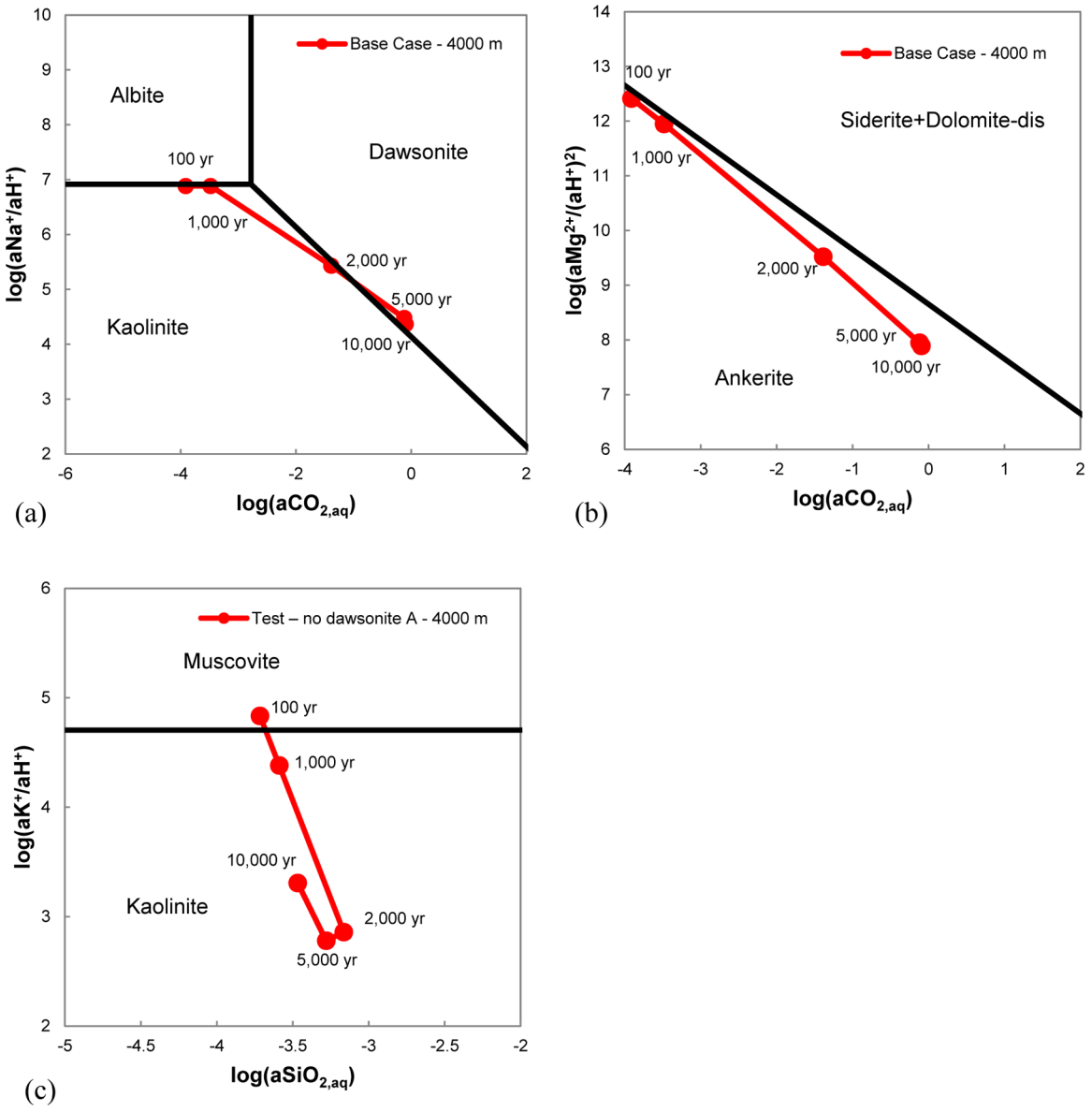

Figure 10. Equilibrium activity−activity diagram at 33.5 °C. Red scatter points are the related data in an increasing time sequence extracted from the Base and "Test−no dawsonite A" cases at 4000 m.

(Figure 10a,b) with the thermodynamic data set used in this study.

The mineral stability diagram (Figure 10a) shows that the reaction path proceeds at the kaolinite−albite boundary during 100−1000 years and enters into the kaolinite stability field during 1000−2000 years. With the increasing $CO_{2,aq}$ concentration due to the acidic brine invasion, the reaction path enters into the dawsonite stability field during ∼2000−10 000 years. Therefore, dawsonite precipitation is much more predominant than kaolinite precipitation during CO_2 sequestration in our simulation (eq 4−7). This is comparable with the results of Gaus et al.[6] and Audigane et al.[56] who found that albite transforms into dawsonite under the conditions of CO_2 storage. Audigane et al.[56] investigated the long-term CO_2 sequestration in the Utsira formation with a 2D reactive transport model, but they did not include ankerite as a secondary carbonate mineral. They found the products of chlorite alteration to be siderite, dolomite, and kaolinite. However, Figure 10b shows that ankerite is thermodynamically more stable than siderite and dolomite in our reactive system; hence, chlorite alteration to ankerite and dawsonite (eq 7) in our modeling results is reasonable.

In addition, we conducted two test cases, "Test−no dawsonite A" and "Test−no dawsonite B" (Table 6) to discuss the influence of dawsonite on long-term CO_2 fate and how it affects the role of rate laws because dawsonite is a rare mineral in nature. Both "Test−no dawsonite A" and "Test−no dawsonite B" exclude dawsonite as a reactive mineral, with all other parameters remaining the same as in the Base and Alex Cases, respectively. The three main coupled reactions in "Test−no dawsonite A" are listed below (eq 8−10).

$$2H^+ + 1K^+ + \underset{\text{albite}}{3NaAlSi_3O_8} \rightarrow \underset{\text{muscovite}}{1KAl_3Si_3O_{10}(OH)_2} + \underset{\text{chalcedony}}{6SiO_2} + 3Na^+ \quad (8)$$

DOI: 10.1021/acs.energyfuels.5b02556
Energy Fuels 2016, 30, 4159−4180

$$2H^+ + 3KAlSi_3O_8 \underset{\text{K-feldspar}}{} \rightarrow 1KAl_3Si_3O_{10}(OH)_2 \underset{\text{muscovite}}{} + 6SiO_2 \underset{\text{chalcedony}}{} + 2K^+ \quad (9)$$

$$4.6H^+ + 1.4K^+ + 7.5CO_{2(aq)} + 2.1Mg_{2.5}Fe_{2.5}Al_2Si_3O_{10}(OH)_8 \underset{\text{chlorite}}{} + 7.5CaCO_3 \underset{\text{calcite}}{} \rightarrow 7.5CaFe_{0.7}Mg_{0.3}(CO_3)_2 \underset{\text{ankerite}}{} + 1.4KAl_3Si_3O_{10}(OH)_2 \underset{\text{muscovite}}{} + 2.1SiO_2 \underset{\text{chalcedony}}{} + 9.3H_2O + 3Mg^{2+} \quad (10)$$

In "Test−no dawsonite A", ankerite becomes the only contributor for mineral trapping, and the alteration product of feldspars changes to muscovite (not kaolinite as expected), compared with the Base Case (eq 4−10; Figure 3 and 4). The mineral stability diagram (Figure 10c) shows that the solution at 4000 m in "Test−no dawsonite A" is located at the kaolinite stability field during ∼2000−10 000 years when the porosity is occupied by the acidic brine. However, muscovite has a larger reactive surface area than kaolinite because of its higher initial abundance (3%); hence, muscovite precipitates faster and becomes one of the main secondary minerals, not kaolinite. At year 5000, the maximum precipitation rate of muscovite in "Test−no dawsonite A" is ∼2.5×10^{-13} mol/kg H_2O/s, which is ∼83 times the value for kaolinite (∼3.0×10^{-15} mol/kg H_2O/s). Because there is no dawsonite precipitation, the porosity in "Test−no dawsonite A" generally increases in the region affected by the CO_2 sequestration (Figure 5). However, the percentage of mineral trapping for the whole domain at year 10 000 decreases from ∼22 to ∼4% (Figure 9a), and the maximum mineral trapping (kg CO_2) in the unit medium at year 10 000 declines from ∼4.9 to ∼1.1 kg/m^3 medium (Figure 9b), compared to the Base Case. In two "no dawsonite" cases, the difference of mineral trapping percentage at year 10 000 between "Test−no dawsonite A" (using LIN law for feldspar dissolution) and "Test−no dawsonite B" (using Alex law for feldspar dissolution) is 1.6%, whereas it is 10% between Base Case and Alex Case where dawsonite is considered (Figure 9c).

5.5. Model Limitations. We used a 1D radial model to investigate the effects of rate laws and regional groundwater flow on long-term CO_2 fate in the present study. Topography and the vertical convective flow are not considered. The ridgelike topography at Sleipner can hinder the effective contact between the brine and the CO_2 plume, only allowing the brine to erode CO_2 gas phase primarily at the bottom of the plume because of the low relative permeability of brine inside the CO_2 plume. Therefore, the 1D radial model used here may overestimate the influence of the groundwater flow to the CO_2 in the structure and the corresponding solubility and mineral trapping.

Vertical brine convection driven by the density difference can extend the vertical distribution of the acidic brine.[80,81] Employing a 1D radial model may underestimate the area covered by the acidic brine in the vertical direction and the corresponding amount of CO_2 trapped into the brine and minerals. A sophisticated 2D or 3D model is needed in the future to investigate the complex interplay of topography (such as dome structure and inclination of sedimentary layer), vertical convective flow, and regional groundwater flow on long-term CO_2 fate.

In addition, using a fresh-brine injection in a radial model to approximately represent regional groundwater flow exaggerates the groundwater velocity near the well and forces the groundwater flow to be radial. These limitations may overstate the washout effect of the groundwater flow on the CO_2 plume (especially near the well) as well as the mixing and dilution effect.

However, the purpose of our study is not to reproduce the multiphase flow phenomenon of the long-term CO_2 disposal in the Utsira Sand accurately. Although the 1D redial model used here has the limitations listed above, the hydrogeological parameters, mineral assemblages, brine composition, CO_2 spill rate into Layer 9, kinetic data, and so on were set on the basis of the observed data or data in the literature. Therefore, our model is appropriate for exploring the general effects of rate laws and regional groundwater flow on long-term CO_2 fate in the sandy aquifer.

5.6. Comparison with Previous Works. Audigane et al.[56] investigated the long-term geological storage of carbon dioxide in the Utsira formation at the Sleipner site with a 2D reactive transport model simulated with TOUGHREACT. The simulation time was 10 000 years and the Utsira formation was approximated as a 2D radially symmetric system with 190 m thickness and two mineralogical assemblages (i.e., a highly permeable sand formation and a semipermeable shale formation represented by four intrathin shale layers). The 2D model considered the ascent of CO_2 plume driven by the buoyance, and it also took into account the vertical brine convection driven by the density difference due to the dissolution of CO_2. However, it did not consider the regional groundwater flow. They found that ∼5% of the injected CO_2 is trapped by minerals at year 10 000 and the remaining is dissolved into the brine. The primary contributors for the mineral trapping in the sands are dawsonite, siderite, and dolomite, and the porosity decreases a little in the sands, <2.5%.

Although the model dimension and thickness and the specific geochemical reactions are different between our model and that in Audigane et al.,[56] the mineral trapping fraction at year 10 000 for the whole domain (∼4%) in our "Test−no water flow A", which does not consider the regional groundwater flow, is comparable with the simulation of Audigane et al.[56] The percentage of mineral trapping at year 10 000 calculated by our Base Case is 22%, which is significantly higher than the value in Audigane et al.[56] This difference is due to the combined effect of the regional groundwater and vertical convective flow. Without regional groundwater flow, the front of acidic brine reaches only as far as ∼3000 m in a horizontal direction in Audigane et al.,[56] whereas the maximum distance the acidic brine reaches in our Base Case is ∼10 000 m. In addition, the concentration of the dissolved CO_2 in the brine at year 10 000 in Audigane et al.[56] is significantly lower because of the effects of convective flow over a larger domain thickness; hence, there is no region of pH < 6.0 at year 10 000 in Audigane et al.[56] In contrast, our Base Case ignores convective flow, so pH still remains at 5.0−5.5 in most of the region in our simulation (Figure 2b). The larger spatial coverage by acidic brine and lower pH values results in a higher mineral trapping fraction in our Base Case than that in Audigane et al.[56]

Audigane et al.[56] did not include ankerite as a secondary carbonate mineral in their model; therefore, Fe, Mg, and Ca released from the dissolution of primary minerals reacted with CO_2 to form siderite and dolomite. However, ankerite is one of

DOI: 10.1021/acs.energyfuels.5b02556
Energy Fuels 2016, 30, 4159−4180

the main contributors for the mineral trapping in our simulation, which is a sink of Fe, Mg, and Ca.

Johnson et al.[58] studied the short-term (20 years) geological storage of carbon dioxide in the Utsira formation with a 2D reactive transport model simulated with NUFT. They evaluated three scenarios with different reservoir heterogeneities, XSH, CSH, and DSH, but they did not consider the regional groundwater flow although their postinjection period was short (~10 years) so this effect should be small. XSH examines a shale-capped homogeneous sandstone aquifer, whereas CSH and DSH impose four intrathin shale layers into XSH. Shales in CSH are laterally continuous and microfractured with a permeability of 3 mD, whereas in DSH they are laterally discontinuous with a permeability of 3 μD, the same as that of the caprock. Johnson et al.[58] found dawsonite, calcite, and magnesite to be the main contributors for the mineral trapping instead of dawsonite and ankerite as in our Base Case because they did not include the Fe-bearing minerals in their model.

Pham et al.[57] investigated how the rate model (BCF+CNT model; CNT: classical nucleation theory), which takes into account both nucleation and growth of secondary carbonate mineral phases, influences the fraction of CO_2 trapped in mineral in a batch system for Utsira-type reservoirs. Their results indicate that only ankerite is the main contributor for mineral trapping. The reason for the differences between Pham et al.[57] and our simulation is that BCF+CNT law considers nucleation processes and that secondary minerals need to overcome a certain threshold SI in order to precipitate, which significantly influences the paragenetic sequence.

6. CONCLUSIONS

To investigate the general effects of rate laws and regional groundwater flow on long-term CO_2 fate in saline aquifers, we constructed a 1D multiphase, coupled reactive mass transport modeling for the uppermost layer (Layer 9) of Utsira Sand formation at the Sleipner site, Norwegian North Sea, using TOUGHREACT. The temporal and spatial evolution of the fate of injected CO_2 at Sleipner, in terms of CO_2 partitioning into the four trapping mechanisms (hydrodynamic/structural, solubility, residual/capillary, and mineral), was simulated with a series of scenarios of reaction kinetics and groundwater flow regimes. The reaction kinetics scenarios feature the combination of a nonlinear rate law for silicate dissolution and a BCF formulation for secondary mineral precipitation, in addition to the commonly used linear rate law for dissolution and precipitation reactions. Although the model dimension and thickness and the specific geochemical reactions are different between our model and previous works on Sleipner, the evolution of mineral trapping is comparable without considering the regional groundwater flow.

We found the following: (1) Changing the dissolution rate laws of the main soluble silicate minerals can influence the silicate reactions and mineral trapping by impacting the sensitivity of the relevant coupled reaction's rate to the acidification of brine. The steeper the slope of the rate$-\Delta G$ relationships, the more sensitive the coupled reaction rate and the mineral trapping are to the acidification of brine. (2) Rate law uncertainties of mineral precipitation have little effect on mineral trapping evolution for Utsira-type formation because the dissolution of primary aluminosilicate minerals are much slower and are the rate-limiters in this case. (3) Soluble silicate minerals can affect mineral trapping directly by coupling with carbonate minerals or indirectly by controlling the related aqueous species concentration (e.g., H^+ and K^+). (4) Neglecting the influence of regional groundwater flow will significantly underestimate the fraction of mineral trapping. This is because fresh brine from upstream continuously erodes CO_2 at the tail of the CO_2 plume, generating a larger area of the acidic brine for mineral trapping. Using the linear dissolution rate law for silicates can exaggerate the effect of groundwater flow on the reaction rates and mineral trapping, compared to using a nonlinear rate law. (5) An increase of the area of acidic brine (e.g., considering the regional groundwater flow, vertical brine convection, or active CO_2 sequestration management) may increase the estimation of the theoretical mineral trapping capacity, but using a linear dissolution rate law for silicates in place of a nonlinear law can overestimate the effect of the acidic brine on the mineral trapping capacity.

AUTHOR INFORMATION

Corresponding Authors

*E-mail: weixiaomei@nwsuaf.edu.cn.

*E-mail: chenzhu@indiana.edu.

Notes

Disclosure: Although the work was partly sponsored by an agency of the United States Government, the views and opinions of authors expressed herein do not necessarily state or reflect those of the United States Government or any agency thereof.

The authors declare no competing financial interest.

ACKNOWLEDGMENTS

We acknowledge the support of the U.S. NSF grant EAR-1225733. Financial support from the China Scholarship Council for G.Z. is also gratefully acknowledged. We thank Sean Miranda for editorial assistance.

REFERENCES

(1) Holloway, S. Underground sequestration of carbon dioxide–a viable greenhouse gas mitigation option. *Energy* **2005**, *30* (11−12), 2318−2333.

(2) Ji, X.; Zhu, C. Chapter 10 - CO_2 storage in deep saline aquifers. In *Novel materials for carbon dioxide mitigation technology*; Morreale, F. S., Ed.; Elsevier: Amsterdam, 2015; pp 299−332.

(3) Bachu, S.; Bonijoly, D.; Bradshaw, J.; Burruss, R.; Holloway, S.; Christensen, N. P.; Mathiassen, O. M. CO_2 storage capacity estimation: Methodology and gaps. *Int. J. Greenhouse Gas Control* **2007**, *1* (4), 430−443.

(4) Metz, B., Davidson, O., de Coninck, H., Loos, M., Meyer, L., Eds. *IPCC Special report on carbon dioxide capture and storage*; Cambridge University Press: Cambridge, U.K., 2005.

(5) Xu, T.; Apps, J. A.; Pruess, K. Numerical simulation of CO_2 disposal by mineral trapping in deep aquifers. *Appl. Geochem.* **2004**, *19* (6), 917−936.

(6) Gaus, I.; Azaroual, M.; Czernichowski-Lauriol, I. Reactive transport modelling of the impact of CO_2 injection on the clayey cap rock at Sleipner (North Sea). *Chem. Geol.* **2005**, *217* (3−4), 319−337.

(7) Xu, T.; Apps, J. A.; Pruess, K. Mineral sequestration of carbon dioxide in a sandstone-shale system. *Chem. Geol.* **2005**, *217*, 295−318.

(8) Zhang, W.; Li, Y.; Xu, T.; Cheng, H.; Zheng, Y.; Xiong, P. Long-term variations of CO_2 trapped in different mechanisms in deep saline formations: a case study of the Songliao Basin, China. *Int. J. Greenhouse Gas Control* **2009**, *3* (2), 161−180.

(9) Balashov, V. N.; Guthrie, G. D.; Hakala, J. A.; Lopano, C. L.; Rimstidt, J. D.; Brantley, S. L. Predictive modeling of CO_2 sequestration in deep saline sandstone reservoirs: Impacts of geochemical kinetics. *Appl. Geochem.* **2013**, *30*, 41−56.

DOI: 10.1021/acs.energyfuels.5b02556
Energy Fuels 2016, 30, 4159−4180

(10) Zhang, L.; Soong, Y.; Dilmore, R.; Lopano, C. Numerical simulation of porosity and permeability evolution of Mount Simon sandstone under geological carbon sequestration conditions. *Chem. Geol.* **2015**, *403*, 1−12.
(11) Schramke, J. A.; Kerrick, D. M.; Lasaga, A. C. The reaction muscovite + quartz ↔ andalusite + K-feldspar + water. Part I. Growth kinetics and mechanism. *Am. J. Sci.* **1987**, *287*, 517−559.
(12) Nagy, K. L.; Blum, A. E.; Lasaga, A. C. Dissolution and precipitation kinetics of kaolinite at 80 °C and pH 3: The effect of deviation from equilibrium. *Am. J. Sci.* **1991**, *291*, 649−686.
(13) Burch, T. E.; Nagy, K. L.; Lasaga, A. C. Free energy dependence of albite dissolution kinetics at 80° C and pH 8.8. *Chem. Geol.* **1993**, *105* (1−3), 137−162.
(14) Gautier, J.-M.; Oelkers, E. H.; Schott, J. Experimental study of K-feldspar dissolution rates as a function of chemical affinity at 150° C and pH 9. *Geochim. Cosmochim. Acta* **1994**, *58*, 4549−4560.
(15) Hellmann, R.; Tisserand, D. Dissolution kinetics as a function of the Gibbs free energy of reaction: An experimental study based on albite feldspar. *Geochim. Cosmochim. Acta* **2006**, *70*, 364−383.
(16) Alekseyev, V. A.; Medvedeva, L. S.; Prisyagina, N. I.; Meshalkin, S. S.; Balabin, A. I. Change in the dissolution rates of alkali feldspars as a result of secondary mineral precipitation and approach to equilibrium. *Geochim. Cosmochim. Acta* **1997**, *61*, 1125−1142.
(17) Taylor, A. S.; Blum, J. D.; Lasaga, A. C. The dependence of labradorite dissolution and Sr isotope release rates on solution saturation state. *Geochim. Cosmochim. Acta* **2000**, *64* (14), 2389−2400.
(18) Zhu, C. Geochemical modeling of reaction paths and geochemical reaction networks. In *Thermodynamics and Kinetics of Water-Rock Interaction*; Oelkers, E. H., Schott, J., Eds.; Mineralogical Society of America: Chantilly, VA, 2009; Vol. *70*, pp 533−569.
(19) Zhu, C.; Lu, P.; Zheng, Z.; Ganor, J. Coupled alkali feldspar dissolution and secondary mineral precipitation in batch systems: 4. Numerical modeling of reaction path and reactive transport. *Geochim. Cosmochim. Acta* **2010**, *74* (14), 3963−3983.
(20) Lu, P.; Konishi, H.; Oelkers, E.; Zhu, C. Coupled alkali feldspar dissolution and secondary mineral precipitation in batch systems: 5. Results of K-feldspar hydrolysis experiments. *Chin. J. Geochem.* **2015**, *34*, 1−12.
(21) Zhu, C.; Blum, A. E.; Veblen, D. R. Feldspar dissolution rates and clay precipitation in the Navajo aquifer at Black Mesa, Arizona, USA. In *Water-Rock Interaction: Proceedings of the Eleventh International Symposium on Water-Rock Interaction WRI-11*; Wanty, R. B.; Seal, R. R. I., Eds.; International Association of GeoChemistry, Saratoga Springs, NY, June 27−July 2, 2004; Taylor & Francis: Boca Raton, FL, 2004; Vol. *2*, pp 895−899.
(22) Zhu, C.; Lu, P. Coupled alkali feldspar dissolution and secondary mineral precipitation in batch systems: 3. Saturation indices of product minerals and reaction paths. *Geochim. Cosmochim. Acta* **2009**, *73*, 3171−3200.
(23) Lu, P.; Fu, Q.; Seyfried, W. E., Jr; Hedges, S. W.; Soong, Y.; Jones, K.; Zhu, C. Coupled alkali feldspar dissolution and secondary mineral precipitation in batch systems − 2: New experiments with supercritical CO_2 and implications for carbon sequestration. *Appl. Geochem.* **2013**, *30*, 75−90.
(24) Fu, Q.; Lu, P.; Konishi, H.; Dilmore, R.; Xu, H.; Seyfried, W. E., Jr; Zhu, C. Coupled alkali-feldspar dissolution and secondary mineral precipitation in batch systems: 1. New experiments at 200 °C and 300 bar. *Chem. Geol.* **2009**, *258* (3−4), 125−135.
(25) Zhang, G.; Lu, P.; Zhang, Y.; Wei, X.; Zhu, C. Effects of rate law formulation on predicting CO_2 sequestration in sandstone formations. *Int. J. Energy Res.* **2015**, *39* (14), 1890−1908.
(26) Liu, F.; Lu, P.; Zhu, C.; Xiao, Y. Coupled reactive flow and transport modeling of CO_2 sequestration in the Mt. Simon sandstone formation, Midwest U.S.A. *Int. J. Greenhouse Gas Control* **2011**, *5* (2), 294−307.
(27) Aradóttir, E. S. P.; Sonnenthal, E. L.; Björnsson, G.; Jónsson, H. Multidimensional reactive transport modeling of CO_2 mineral sequestration in basalts at the Hellisheidi geothermal field, Iceland. *Int. J. Greenhouse Gas Control* **2012**, *9*, 24−40.
(28) Tutolo, B. M.; Kong, X.-Z.; Seyfried, W. E.; Saar, M. O. High performance reactive transport simulations examining the effects of thermal, hydraulic, and chemical (THC) gradients on fluid injectivity at carbonate CCUS reservoir scales. *Int. J. Greenhouse Gas Control* **2015**, *39*, 285−301.
(29) Hermanrud, C.; Andresen, T.; Eiken, O.; Hansen, H.; Janbu, A.; Lippard, J.; Bolås, H. N.; Simmenes, T. H.; Teige, G. M. G.; Østmo, S. Storage of CO_2 in saline aquifers-lessons learned from 10 years of injection into the Utsira Formation in the Sleipner area. *Energy Procedia* **2009**, *1* (1), 1997−2004.
(30) NRC. *Induced seismicity potential in energy technologies*; National Academies Press: Washington, DC, 2013.
(31) Zhu, C.; Zhang, G.; Lu, P.; Meng, L.; Ji, X. Benchmark modeling of the Sleipner CO_2 plume: Calibration to seismic data for the uppermost layer and model sensitivity analysis. *Int. J. Greenhouse Gas Control* **2015**, *43*, 233−246.
(32) Zhang, G.; Lu, P.; Zhu, C. Model predictions via history matching of CO_2 plume migration at the Sleipner Project, Norwegian North Sea. *Energy Procedia* **2014**, *63*, 3000−3011.
(33) Lasaga, A. C. Rate laws of chemical reactions. In *Kinetics of Geochemical Processes*; Lasaga, A. C., Kirkpatrick, R. J., Ed.; Mineralogical Society of America: Washington, DC, 1981; Vol. *8*, pp 1−68.
(34) Lasaga, A. C. Transition state theory. In *Kinetics of Geochemical Processes*; Lasaga, A. C.; Kirkpatrick, R. J., Eds.; Mineralogical Society of America: Washington, DC, 1981; Vol. *8*, pp 135−169.
(35) Aagaard, P.; Helgeson, H. C. Thermodynamic and kinetic constraints on reaction rates among minerals and aqueous solutions. I. Theoretical considerations. *Am. J. Sci.* **1982**, *282*, 237−285.
(36) Burton, W. K.; Cabrera, N.; Frank, F. C. The growth of crystals and the equilibrium structure of their surfaces. *Philos. Trans. R. Soc., A* **1951**, *243*, 299−358.
(37) Baklid, A.; Korbol, R.; Owren, G. Sleipner Vest CO_2 disposal, CO_2 injection into a shallpow underground aquifer. *SPE Annual Technical Conference and Exhibition, Denver, Colorado, USA*, 1996.
(38) Zweigel, P.; Arts, R.; Lothe, A. E.; Lindeberg, E. B. G. Reservoir geology of the Utsira Formation at the first industrial-scale underground CO_2 storage site (Sleipner area, North Sea). *Geol. Soc. Spec. Publ.* **2004**, *233* (1), 165−180.
(39) Singh, V.; Cavanagh, A.; Hansen, H.; Nazarian, B.; Iding, M.; Ringrose, P. Reservoir modeling of CO_2 plume behavior calibrated against monitoring data from Sleipner, Norway. *SPE Annual Technical Conference and Exhibition, Florence, Italy*, 2010.
(40) Chadwick, R. A.; Arts, R.; Eiken, O. 4D seismic quantification of a growing CO_2 plume at Sleipner, North Sea. *Petroleum, Geology Conference series, January 1, 2005*, Geological Society: London, 2005.
(41) Holloway, S.; Chadwick, A.; Czernichowski-Lauriol, I.; Arts, R. *Best practice manual from SACS - scaling aquifer CO_2 storage project*; IEA Greenhouse Gas R&D Programme, Schlumberger Research, European Commission: Trondheim, Norway, 2005; p 53.
(42) Chadwick, R. A.; Noy, D.; Arts, R.; Eiken, O. Latest time-lapse seismic data from Sleipner yield new insights into CO_2 plume development. *Energy Procedia* **2009**, *1* (1), 2103−2110.
(43) Chadwick, A.; Noy, D. Time-lapse seismic monitoring at Sleipner: insights into the performance of reservoir seals. *Workshop on Caprocks and Seals in Geological Carbon Sequestration, Pacific Groove, CA*, 2010.
(44) Boait, F. C.; White, N. J.; Bickle, M. J.; Chadwick, R. A.; Neufeld, J. A.; Huppert, H. E. Spatial and temporal evolution of injected CO_2 at the Sleipner Field, North Sea. *J. Geophys. Res.* **2012**, *117*, B03309.
(45) Cavanagh, A. Benchmark calibration and prediction of the Sleipner CO_2 plume from 2006 to 2012. *Energy Procedia* **2013**, *37* (0), 3529−3545.
(46) Chadwick, R. A.; Noy, D. J. History-matching flow simulations and time-lapse seismic data from the Sleipner CO_2 plume. *Geological Society, London, Petroleum Geology Conference series* **2010**, *7*, 1171−1182.

DOI: 10.1021/acs.energyfuels.5b02556
Energy Fuels 2016, 30, 4159−4180

(47) Garven, G. A hydrogeologic model for the formation of the giant oil sands deposits of the Western Canada sedimentary basin. *Am. J. Sci.* **1989**, *289* (2), 105−166.
(48) Garven, G. Continental-scale groundwater flow and geologic processes. *Annu. Rev. Earth Planet. Sci.* **1995**, *23*, 89−118.
(49) Xu, T.; Sonnenthal, E.; Spycher, N.; Pruess, K. *TOUGHREACT user's guide: A simulation program for non-isothermal multiphase reactive geochemical transport in variably saturated geologic media*, V1.2; Lawrence Berkeley National Laboratory: Berkeley, CA, 2004.
(50) Pruess, K.; *ECO$_2$N: A TOUGH2 fluid property module for mixtures of water, NaCl, and CO$_2$*; Earth Sciences Division, Lawrence Berkeley National Laboratory: Berkley, CA, 2005.
(51) Lasaga, A. C.; Soler, J. M.; Ganor, J.; Burch, T. E.; Nagy, K. L. Chemical weathering rate laws and global geochemical cycles. *Geochim. Cosmochim. Acta* **1994**, *58* (10), 2361−2386.
(52) André, L.; Azaroual, M.; Menjoz, A. Numerical simulations of the thermal impact of supercritical CO_2 injection on chemical reactivity in a carbonate saline reservoir. *Transp. Porous Media* **2010**, *82* (1), 247−274.
(53) Pruess, K.; Olderburg, C.; Moridis, G. *TOUGH2 user's guide*, version 2.0; Lawrence Berkeley National Laboratory: Berkley, CA, 2012.
(54) Pearce, J. M.; Kemp, S. J.; Wetton, P. D. *Mineralogical and petrographical characterization of 1m core from the Utsira formation, Central North Sea*; British Geological Survey: Keyworth, U.K., 1999.
(55) Chadwick, R. A.; Zweigel, P.; Gregersen, U.; Kirby, G. A.; Holloway, S.; Johannessen, P. N. Geological reservoir characterization of a CO_2 storage site: the Utsira Sand, Sleipner, northern North Sea. *Energy* **2004**, *29* (9−10), 1371−1381.
(56) Audigane, P.; Gaus, I.; Czernichowski-Lauriol, I.; Pruess, K.; Xu, T. F. Two-dimensional reactive transport modeling of CO_2 injection in a saline aquifer at the Sleipner site, North Sea. *Am. J. Sci.* **2007**, *307*, 974−1008.
(57) Pham, V. T. H.; Lu, P.; Aagaard, P.; Zhu, C.; Hellevang, H. On the potential of CO_2−water−rock interactions for CO_2 storage using a modified kinetic model. *Int. J. Greenhouse Gas Control* **2011**, *5* (4), 1002−1015.
(58) Johnson, J. W.; Nitao, J. J.; Knauss, K. G. Reactive transport modelling of CO_2 storage in saline aquifers to elucidate fundamental processes, trapping mechanisms and sequestration partitioning. *Geol. Soc. Spec. Publ.* **2004**, *233* (1), 107−128.
(59) Xu, T.; Sonnenthal, E.; Spycher, N.; Pruess, K. TOUGHREACT–A simulation program for non-isothermal multiphase reactive geochemical transport in variably saturated geologic media: Applications to geothermal injectivity and CO_2 geological sequestration. *Comput. Geosci.* **2006**, *32* (2), 145−165.
(60) Wolery, T. J. *EQ3/6, A software package for geochemical modeling of aqueous systems: Package overview and installation guide* (version 7.0); Lawrence Livermore National Laboratory: Berkley, CA, 1992; p 41.
(61) Arnorsson, S.; Stefansson, A. Assessment of feldspar solubility constants in water in the range of 0 degrees to 350 degrees C at vapor saturation pressures. *Am. J. Sci.* **1999**, *299* (3), 173−209.
(62) Stefansson, A.; Arnórsson, S. Feldspar saturation state in natural water. *Geochim. Cosmochim. Acta* **2000**, *64* (15), 2567−2584.
(63) Yates, D. M.; Rosenberg, P. E. Formation and stability of endmember illite: II. Solution equilibration experiments at 100−250 °C and $P_{v,soln}$. *Geochim. Cosmochim. Acta* **1997**, *61* (15), 3135−3144.
(64) Ferrante, M. J.; Stuve, J. M.; Richardson, D. W. *Thermodynamic data for synthetic Dawsonite*; U.S. Department of the Interior, Bureau of Mines: Washington, DC, 1976.
(65) Rock, P. A.; Mandell, G. K.; Casey, W. H.; Walling, E. M. Gibbs energy of formation of dolomite from electrochemical cell measurements and theoretical calculations. *Am. J. Sci.* **2001**, *301* (2), 103−111.
(66) Preis, W.; Gamsjager, H. Critical evaluation of solubility data: enthalpy of formation of siderite. *Phys. Chem. Chem. Phys.* **2002**, *4*, 4014−4019.
(67) Rimstidt, J. D. Quartz solubility at low temperatures. *Geochim. Cosmochim. Acta* **1997**, *61* (13), 2553−2558.
(68) Mohd Amin, S.; Weiss, D. J.; Blunt, M. J. Reactive transport modelling of geologic CO_2 sequestration in saline aquifers: The influence of pure CO_2 and of mixtures of CO_2 with CH_4 on the sealing capacity of cap rock at 37 °C and 100 bar. *Chem. Geol.* **2014**, *367*, 39−50.
(69) Palandri, J. L.; Kharaka, Y. K. *A compilation of rate parameters of water-mineral interaction kinetics for application to geochemical modeling*; U.S. Geological Survey: Washington, DC, 2004; p 66.
(70) Steefel, C. I. *CRUNCH*; Lawrence Livermore National Laboratory: Berkley, CA, 2001; p 76.
(71) Xu, T.; Kharaka, Y. K.; Doughty, C.; Freifeld, B. M.; Daley, T. M. Reactive transport modeling to study changes in water chemistry induced by CO_2 injection at the Frio-I Brine Pilot. *Chem. Geol.* **2010**, *271* (3−4), 153−164.
(72) Sonnenthal, E. L.; Spycher, N. *Drift-scale coupled processes (DST and THC seepage) models*; Yucca Mountain Project: Las Vegas, NV, 2001.
(73) Johnson, J. W. Structural, compositional, and process controls on the dynamic mass partitioning and spatial distribution of CO_2 trapping mechanisms: Influence on isolation performance. *Energy Procedia* **2009**, *1* (1), 3499−3506.
(74) Maher, K.; Steefel, C. I.; White, A. F.; Stonestrom, D. A. The role of reaction affinity and secondary minerals in regulating chemical weathering rates at the Santa Cruz Soil Chronosequence, California. *Geochim. Cosmochim. Acta* **2009**, *73* (10), 2804−2831.
(75) Zhu, C. Current status of geochemical modeling in environmental and geological studies. In *Encyclopedia of sustainability science and technology*; Meyers, R. A., Ed.; Springer: New York, 2013.
(76) Zhang, S.; Yang, L.; DePaolo, D. J.; Steefel, C. I. Chemical affinity and pH effects on chlorite dissolution kinetics under geological CO_2 sequestration related conditions. *Chem. Geol.* **2015**, *396* (0), 208−217.
(77) Zhu, J.; Parris, T. M.; Bowersox, J. R.; Harris, D. C. Modeling CO_2−brine−rock interactions in the Knox Group: Implications of a deep carbon storage field test in western Kentucky. *Appl. Geochem.* **2013**, *37*, 29−42.
(78) Beni, A. N.; Clauser, C. The influence of temperature on chemical fluid-rock reactions in geological CO_2 sequestration. *Environmental Modeling & Assessment* **2014**, *19* (4), 315−324.
(79) Xu, T.; Apps, J. A.; Pruess, K. Reactive geochemical transport simulation to study mineral trapping for CO_2 disposal in deep arenaceous formations. *J. Geophys. Res.* **2003**, *108* (B2), 2071.
(80) Ennis-King, J.; Paterson, L. Coupling of geochemical reactions and convective mixing in the long-term geological storage of carbon dioxide. *Int. J. Greenhouse Gas Control* **2007**, *1* (1), 86−93.
(81) Hidalgo, J. J.; Carrera, J. Effect of dispersion on the onset of convection during CO_2 sequestration. *J. Fluid Mech.* **2009**, *640*, 441−452.
(82) Boait, F.; White, N.; Chadwick, A.; Noy, D.; Bickle, M. Layer spreading and dimming within the CO_2 plume at the sleipner field in the north sea. *Energy Procedia* **2011**, *4* (0), 3254−3261.
(83) Cavanagh, A. J.; Haszeldine, R. S. The Sleipner storage site: Capillary flow modeling of a layered CO_2 plume requires fractured shale barriers within the Utsira Formation. *Int. J. Greenhouse Gas Control* **2014**, *21* (0), 101−112.
(84) Van Genuchten, M. T. A closed-form equation for predicting the hydraulic conductivity of unsaturated soils. *Soil Sci. Soc. Am. J.* **1980**, *44* (5), 892−898.
(85) Corey, A. T. The interrelation between gas and oil relative permeabilities. *Producers Monthly* **1954**, *19* (1), 38−41.
(86) Bickle, M.; Chadwick, A.; Huppert, H. E.; Hallworth, M.; Lyle, S. Modelling carbon dioxide accumulation at Sleipner: implications for underground carbon storage. *Earth Planet. Sci. Lett.* **2007**, *255* (1−2), 164−176.

DOI: 10.1021/acs.energyfuels.5b02556
Energy Fuels 2016, 30, 4159−4180